University of New Mexico
UNM Digital Repository

Biology ETDs | Electronic Theses and Dissertations

12-1-2014

# Bridging structure and function in semi-arid ecosystems by integrating remote sensing and ground based measurements

Dan Krofcheck

Follow this and additional works at: https://digitalrepository.unm.edu/biol_etds

Recommended Citation
Krofcheck, Dan. "Bridging structure and function in semi-arid ecosystems by integrating remote sensing and ground based measurements." (2014). https://digitalrepository.unm.edu/biol_etds/67

This Dissertation is brought to you for free and open access by the Electronic Theses and Dissertations at UNM Digital Repository. It has been accepted for inclusion in Biology ETDs by an authorized administrator of UNM Digital Repository. For more information, please contact disc@unm.edu.

Dan J. Krofcheck

*Candidate*

Biology

*Department*

This dissertation is approved, and it is acceptable in quality and form for publication:

*Approved by the Dissertation Committee:*

Marcy Litvak , Chairperson

William Pockman

Chris Lippitt

Jan Eitel

Nate McDowell

# Bridging structure and function in semi-arid ecosystems by integrating remote sensing and ground based measurements

by

**Dan J. Krofcheck**

B.S. Chemistry, Environental Studies, Ohio Wesleyan University, 2009

DISSERTATION

Submitted in Partial Fulfillment of the
Requirements for the Degree of

Doctor of Philosophy
Biology

The University of New Mexico

Albuquerque, New Mexico

December 2014

©2014, Dan J. Krofcheck

# Acknowledgments

The research in chapter 2 was funded by the DOE BER grant DE-FOA-0000536. Chapter 3 was funded by both the DOE BER award as well as funds awarded by the New Mexico Space Grant Consortium, and chapter 4 was funded by NASA award NNX11AG91G. Several annual grants and scholarships from the Department of Biology at the University of New Mexico offset travel and conference fees throughout the project.

I wish to thank the Litvak Lab research crew for experiment and data management support, as well as the professors and students that have made this an enjoyable experience.

# Bridging structure and function in semi-arid ecosystems by integrating remote sensing and ground based measurements

by

**Dan J. Krofcheck**

B.S. Chemistry, Environental Studies, Ohio Wesleyan University, 2009

Ph.D Biology, University of New Mexico, 2014

## Abstract

The Southwestern US is projected to continue the current significant warming trend, with increased variability in the timing and magnitude of rainfall events. The effects of these changes in climate are already evident in the form of multi-year droughts which have resulted in the widespread mortality of woody vegetation across the region. Therefore, the need to monitor and model forest mortality and carbon dynamics at the landscape and regional scale is an essential component of regional and global climate mitigation strategies, and critical if we are to understand how the imminent state transitions taking place in forests globally will affect climate forcing and feedbacks. Remote sensing offers the only solution to multitemporal regional observation, yet many challenges exist with employing modern remote sensing solutions in highly stressed vegetation characteristic of semi-arid biomes, making one of the most expansive biomes on the globe also one of the most difficult to accurately monitor and model. The goal of this research was to investigate how changes

in the structure of semi-arid woodlands following forest mortality impacts ecosystem function, and to determine how this question can be addressed using remotely sensed data sets. I focused primarily on Pinus edulis and Juniperous monosperma (piñon-juniper) woodlands, and took advantage of an existing manipulation experiment where mortality was imposed on all of the large piñon (¡ 7 cm dbh) in a 4 ha PJ woodland in 2009 and the ecosystem functional responses have been quantified using eddy covariance. A nearby intact PJ woodland, also instrumented with eddy covariance, was used as a control for this experiment. I tested the ability of high resolution remote sensing data to mechanistically describe the patterns in overstory mortality and understory green-up in this manipulated woodland by comparing it to the intact woodland, and observed the heterogeneous response of the understory as a function of cover type. I also investigated the relationship between changes in soil water content and the greenness of the canopy, noting that in the disturbed woodland, I observed a decoupling between how the canopy was measured remotely (e.g., via vegetation indices, VI) and photosynthesis. This is significant in that it potentially represents a significant source of error in using existing light use efficiency models of carbon uptake in these disturbed woodlands. This research also suggested that leveraging remote sensing data which measures in the red-edge portion of reflected light can provide increased sensitivity to the low leaf area, ephemeral pulses of greenup that were identified in the disturbed woodland, post-canopy mortality. Given these findings, I developed a hierarchy of simple linear models to test how well vegetation indices acquired through different spatial resolution sensors (Landsat and RapidEye) were able to predict carbon uptake in both intact and disturbed piñon-juniper woodlands. The vegetation indices used were a moisture sensitive VI, and a red-edge leveraging VI from these sensors, and I compared estimates of carbon uptake derived from these models to the Gross Primary Productivity estimated from tower-based eddy covariance at both the manipulated and intact piñon-juniper sites. I determined that the red-edge VI and the moisture sensitive VI both constrained

uncertainty associated with carbon uptake, but that the variability in satellite view angle from scene to scene can impose a significant amount of noise in sparse canopy ecosystems. Finally, given the extent and prevalence of J. monosperma across the region, and its complex growth morphology, I tested the ability of aerial lidar to quantify the biomass of juniper. In this simplified case study, I developed a methodology to relate the volume of canopy measured via lidar to the equivalent stem area at the root crown. By working in a single species ecosystem, I circumvented many challenges associated with driving allometries remotely, but also present a work-flow that I intend to adapt to more complex systems, namely piñon-juniper woodlands. Together, this work describes and addresses existing challenges with respect to using remote sensing to understand both the structure and function of piñon-juniper woodlands, and how it changes in response to widespread piñon mortality. It provides several new techniques to mitigate the difficulties associated with monitoring mortality / recovery dynamics, predicting canopy function, and determining ecosystem state parameters in these complex, sensitive biomes.

# Contents

**List of Figures** **xiii**

**List of Tables** **xviii**

**1 Introduction** **1**

**2 Detecting mortality induced structural and functional changes in piñon-juniper woodland using Landsat and RapidEye time series** **7**

2.1 Introduction . . . . . 7

2.2 Methods . . . . . 11

2.2.1 Site Description . . . . . 11

2.2.2 In situ field measurements . . . . . 12

2.2.3 Plot level vegetation sampling . . . . . 13

2.2.4 Remote sensing image data and pre-processing . . . . . 14

2.2.5 Pixel Extraction . . . . . 15

2.2.6 Vegetation Index Selection . . . . . 16

2.3 Results . . . . . 18

2.3.1 Overstory vegetation structure changes and ecosystem productivity . . . . . 18

2.3.2 3.2 Understory vegetation structural changes and ecosystem productivity . . . . . 20

2.3.3 Uncoupling of canopy reflectance and ecosystem function . . . 25

2.4 Discussion . . . . . 27

2.4.1 Utility of time series imagery for canopy structural change detection . . . . . 27

2.4.2 Higher spatial resolution imagery aids semi-arid canopy change detection . . . . . 29

2.4.3 Monitoring the function of semi-arid biomes using satellite imagery hinges on water availability . . . . . 30

2.5 Conclusions . . . . . 31

**3 Remote sensing based simple models of GPP in both disturbed and undisturbed piñon-Juniper woodlands in the Southwestern U.S. 34**

3.1 Introduction . . . . . 34

3.2 Methodology . . . . . 37

3.2.1 Site Description . . . . . 37

3.2.2 Data: gross primary productivity . . . . . 39

3.2.3 Data: Landsat ETM+ . . . . . 40

3.2.4 Data: RapidEye . . . . . 41

3.2.5 Spectral vegetation indices . . . . . 41

3.2.6 Statistical analysis . . . . . 42

3.3 Results and Discussion . . . . . 43

3.3.1 Models of GPP in PJ woodlands had the lowest error at the disturbed site . . . . . 43

3.3.2 NDRE and NDWI reduced model error only during periods of significant stress . . . . . 45

3.3.3 Inconsistency in sensor view imposed significant variability RapidEye VI model performance . . . . . 48

3.3.4 Implications for regional remote sensing based estimations of GPP in PJ woodlands . . . . . 50

3.3.5 Conclusions . . . . . 52

**4 Woody biomass estimation in a Southwestern US juniper savanna using clumped tree segmentation and existing allometries. 55**

4.1 Introduction . . . . . 55

4.2 Methods . . . . . 59

4.2.1 Site description . . . . . 59

4.2.2 Field measurements . . . . . 59

4.2.3 Airborne lidar data . . . . . 61

4.2.4 Canopy segementation and statistics . . . . . 61

4.2.5 Validation of clump level allometrics . . . . . 64

4.2.6 Uncertainty analysis . . . . . 65

4.3 Results . . . . . 66

4.3.1 Field Measurements . . . . . 66

4.3.2 Lidar Segmentation . . . . . 66

4.3.3 Segmentation derived biomass and uncertainty . . . . . 68

4.4 Discussion . . . . . 70

4.5 Conclusions . . . . . 74

**5 Conclusions** **76**

# List of Figures

2.1 The study sites are located < 3 km apart from eachother in central New Mexico. The extent of piñon-juniper woodland across the state is shown in green. . . . . 11

2.2 A phenocam placed atop the flux tower at the girdled manipulation site provides a timeline of major, visible structural change that took place following the manipulation, from before the manipulation took place (top) to total loss of needles on all manipulated trees (bottom). 17

2.3 Cumulative gross primary productivity throughout the manipulation for both the control (gray) and girdle (black) sites. The time of the girdling is marked with a vertical dashed line. . . . . 19

2.4 Time series of A) gross primary productivity measured at the flux tower, B) Landsat ETM+ derived NDVI, and C) RapidEye NDVI, for both the control (gray) and girdle (black)sites. . . . . 20

2.5 RapidEye derived cover specific responses for the girdled trees (closed circles) and the spaces between girdled trees (open squares). The data are normalized relative to the control site: positive values indicate the index is greater at control. . . . . 21

2.6 Forb density before and following the manipulation at both the control (gray) and girdle (black) sites. Outliers are plotted as points, and are defined as values which are 1.5 times greater than the 75th percentile. Significance $^*P < 0.001$ is marked by an asterisk. . . . . 22

2.7 Fetch-wide relationship between canopy vegetation indices and soil volumetric water content during periods where temperature and soil moisture are least limiting plant productivity (air temperature > 0C or soilmoisture < 9%). . . . . 23

2.8 Fetch-wide relationship between canopy vegetation indices and soil volumetric water content during periods where temperature and soil moisture are most limiting plant productivity (air temperature < 0C or soilmoisture < 9%). . . . . 24

2.9 Fetch-wide relationship between gross primary productivity and canopy vegetation indices during periods where temperature and soil moisture are least limiting plant productivity (air temperature > 0C or soilmoisture > 9%). . . . . 25

2.10 Fetch-wide relationship between gross primary productivity and canopy vegetation indices during periods where temperature and soil moisture are most limiting plant productivity (air temperature < 0C or soilmoisture < 9%). . . . . 26

2.11 Fetch-wide relationship between gross primary productivity and soil water content during growing (temperature > 0C or soil mousture > 9%) and growth limited (air temperature < 0C or soilmoisture < 9%) conditions. . . . . 27

*List of Figures*

3.1 The study sites are located < 3 km apart from eachother in central New Mexico. The extent of piñon-juniper woodland across the state is shown in green. . . . . 38

3.2 Linear model fit 1:1 curves for all model forms in the hierarchy. Data for the control and girdle sites are fit independently (left and right columns respectively). LS and RE denote Landsat and RapidEye. . 44

3.3 Linear model fit 1:1 curves for all model forms in the hierarchy, parameterized with only data from 2009. Data for the control and girdle sites are fit independently (left and right columns respectively). LS and RE denote Landsat and RapidEye. . . . . 46

3.4 (A) RapidEye false color composites of the PJ control site (top), and the corresponding fraction of pixels with NDVI ¿ 0.30 (bottom), with detailed subsets on the far right. (B) Histogram of view angles that comprised the entire RapidEye time series. View angles are represented as absolute values from nadir. . . . . 49

3.5 Linear model fit 1:1 curves for all model forms in the hierarchy, parameterized with only data corresponding to dates on which RapidEye imagesvwere acquired at view angles <= +/- 7 degrees from nadir. Data for the control and girdle sites are fit independently (left and right columns respectively). LS and RE denote Landsat and RapidEye. . . . . 51

4.1 (A) Extent of pinon juniper woodlands (dark green) and juniper savanna (light green) ecosystems across the four corner states. (B) Location and layout of the field site, with tree crown locations bounded by the four 17.5 m radius circle plots. . . . . 58

4.2 Example growth morphology of a typical oneseed juniper. The multiple branching in this example occurs above the ground level. . . . . 60

4.3 Lidar canopy height acquisition extent (A) with the 4 hectare study region identified by the extent indicator (B). The corresponding TEXPERT segmentation (C) delineated isolated and clumped crowns. . . 62

4.4 (A) The automatic delineation of ground and vegetation from TEXAS model, resulting in (B) clumped crown segmentation which was then (C) vectorized and overlayed on ground measured stem maps within our study area for segment statistic generation. . . . . 63

4.5 Distributions of juniper canopy parameters retrieved via ground measurement. . . . . 65

4.6 Distributions of tree heights from the imagery extent (left) and the Field validation plots (right). A vertical dashed line marks the mean (mu) of each Distribution. . . . . 67

4.7 Ground derived relationships between equivalent stem diameter (see eqn. 1), and three remotely retrievable canopy parameters. Both axes have been log transformed to generate linear fits. . . . . 68

4.8 Field estimates of canopy height for the 52 trees sampled in The study. Lidar heights were manually extracted from the corresponding Crowns. . . . . 69

4.9 Remotely retrieved crown clump equivalent stem density (ESD) regressed against measured stem density within each clump (A) with canopy closure (B) and canopy density (C) as regression covariates. . 69

4.10 Relationship between the estimated segment biomass and the corresponding Monte-Carlo derived estimation of segment biomass standard deviation. . . . . 70

4.11 Mean (A) and Variance (B) of segment biomass across the analysis extent, spatially averaged for visualization. Corresponding detail subsets of individual segment mean and variance (C and D respectively). . . . . 71

# List of Tables

3.1 Adjusted AIC and adjusted R2 fit statistics for all model forms in the hierarchy, parameterized using the entire data set, from the Fall of 2009 to the Winter of 2011. . . . . 45

3.2 Adjusted AIC and adjusted R2 fit statistics for all model forms in the hierarchy, parameterized using only data from 2009 . . . . . 47

3.3 Adjusted AIC and adjusted R2 fit statistics for all model forms in the hierarchy, parameterized using only data corresponding to dates on which RapidEye images were acquired at view angles <= +/- 7 degrees from nadir. . . . . 50

4.1 Summary of the clumped segmentation statistics generated from the full 3D point cloud for all of the canopy objects within the analysis extent. . . . . 73

# Chapter 1

# Introduction

Semi-arid ecosystems play an important, often pivotal, role in influencing the global carbon budget (Poulter et al, 2014). With ecosystem properties characteristic of low productivity biomes (e.g., low leaf area index and low vegetation fractional cover), these regions normally experience highly variable precipitation and temperature regimes which impose constant hydraulic stress on the vegetation, testing the ability of plant adaptation to cope with challenging abiotic conditions. While anomalous increases in precipitation in these regions can result in massive contributions to global carbon uptake (e.g., (Poulter et al, 2014), the converse is true for regions which experience climate change related droughts, which increase the extent, severity, and duration of conditions that stress vegetation, placing an expansive and already sensitive set of ecosystems at an ecological tipping point. In the Southwestern US, the latter is the case, with widespread woody mortality events already highly correlated with persistent, severe drought, turning wide expanses of woodland into mixed stands of live and dead vegetation. The structural changes that follow forest mortality may result in potentially large and yet unquantified impacts on ecosystem carbon uptake. This dissertation investigates the relationship between changes in ecosystem structure and ecosystem function in the Southwestern US, from the perspective of

leveraging remote sensing capabilities to scale local measurements to landscapes and regions.

Recent changes in climate projected for the Southwestern US have shown strong consensus throughout the literature (e.g., (IPCC 2007; Seager et al 2007), and have grown in confidence given the changes already realized at the national level (e.g., IPCC 2014, National Climate Assessment, 2014). Increases in air temperature, coupled with increased variability of less frequent rain events has the Southwestern US staged for an imminent transition towards hotter, drier conditions which result in woody mortality (Williams et al, 2010; Allen et al, 2010; McDowell, 2011; Williams et al, 2012), increasing the need for rapid monitoring systems capable of resolving the changes taking place in semi-arid regions both spatially, and temporally McDowell et al., 2014, in review).

Remote sensing provides the only means by which landscapes at national and global scales can be observed repeatedly, leveraging unique reflectance properties of vegetation to predict vegetation function, usually gross primary productivity (GPP) (e.g., (Running et al, 1999; Zhao et al, 2011)). These approaches generally rely on vegetation indices (VI) which leverage various portions of vegetation reflectance spectra that are sensitive to components of vegetation chemical composition (e.g., chlorophyll content) and structure (e.g., leaf area) in order to probe some aspect of vegetation structure (e.g., leaf area), or function (e.g., photosynthesis). The latter historically has been estimated using a light use efficiency approach ((Monteith, 1972; Monteith and Moss, 1977)). The success of widely applied remote sensing based models of GPP perform poorly in semi-arid ecosystems, given the low spectral response of the vegetation due to persistent drought, and low vegetation fractional cover. Consequently, some of the most widespread terrestrial ecosystems globally also have some of the greatest uncertainty associated with their function.

The most common ecosystem in the Southwestern US, piñon-juniper (PJ) wood-

lands, are a model biome for investigating the impacts of ecosystem structural changes post mortality on the subsequent function of that ecosystem. Ground based measurements for chapters 2 and 3 came from a pair of experimental PJ woodlands located in central NM. This paired site experiment monitored in-situ carbon flux using eddy-covariance during a simulated mortality event, wherein all of the adult piñon pine at one of the 4 ha sites were mechanically and chemically girdled. The resulting timeline of tree mortality, defoliation rates, and stand structure were very representative of post PJ mortality stand demographics typical of the region (Clifford et al, 2008; Royer et al, 2011; Clifford et al, 2013).

In chapter 2 (Krofcheck et al, 2014), we leveraged a time series of spatially and temporally resolved remote sensing data from the RapidEye satellite constellation to quantify the effects of the piñon mortality relative to the nearby control site. The main function afforded by the RapidEye sensor platform was that we were able to stratify our analysis by cover type, and look at the VI response of girdled piñon crowns, surviving juniper, and the inter-crown regions. Further, we were able to leverage the red-edge waveband on the sensor as a means to calculate the normalized difference red-edge index (NDRE), which previously had been shown to be more sensitive to changes in canopy chlorophyll than the traditionally employed normalized difference vegetation index (NDVI) (Eitel et al, 2011). The moderate resolution of Landsat 7 ETM+ (30 x 30 meter pixels) tracked the decrease in NDVI at the girdled site relative to the control fairly well at the scale of the experimental region. The RapidEye data however indicated that just 2 years following the manipulation, herbaceous, ephemeral vegetation was establishing underneath the girdled crowns and offsetting the decrease in NDVI viewed remotely. The NDRE was more sensitive to these post-mortality transitions, furthering the idea that NDRE may play a role in the early detection of not only stress onset but also ecosystem recovery from stress. We also determined that by the end of the experiment, changes in the VI at the girdled site were more responsive to changes in soil water content than at the control

site, most likely attributed to the changes in herbaceous leaf area as a precipitation pulse driven phenomenon.

Tracking the structural changes imposed on the PJ experiment following the manipulation prompted the work in chapter 3, which took the two main findings from chapter 2 and incorporated them into a simple model hierarchy. My results from chapter 2 suggested that a variety of VI can be used to monitor ecosystem stress and recovery patterns and high to medium resolution, and that water availability in these systems was a primary driver of both the gross function of canopies and the ephemeral green-up of inter-crown and understory vegetation. In chapter 3, I tested the ability of NDRE to predict Gross Primary Productivity (total carbon uptake, or GPP) when combined with air temperature and photosynthetically active radiation. I also investigated the ability of the normalized difference wetness index (NDWI) to constrain model error during periods of drought. By combining the results of five linear models at each site, validated against the in-situ measures of carbon flux, I determined that including NDWI generally improved model performance, serving to support the intuitive hypothesis that VI which contain information about surface wetness can aid in the modeling of GPP in semi-arid biomes. NDRE from RapidEye was a better predictor of GPP at the girdled site than NDVI from the same sensor, but the cross sensor comparisons (i.e., RapidEye vs Landsat 7 ETM+) were significantly confounded by variability in view-angle and sensor geometry of the RapidEye data set. Regardless of this complication, I believe that given the previously established ability of NDRE to track changes in canopy chlorophyll due to stress onset (Eitel et al, 2011), and the increased performance over NDVI with respect to monitoring ephemeral green-up following disturbance (Krofcheck et al, 2014), NDRE should be considered as a VI used to model GPP in semi-arid regions, especially during the onset of or recovery from woody mortality.

The experimental manipulation which drove chapters 2 and 3 left the girdled

site functioning like a juniper savanna, both in terms of cumulative carbon uptake and ecosystem light response. In the fall of 2013, significant mortality of piñon pine across our entire experimental plateau began to occur, as the cumulative effects of increased drought pressure and bark beetle outbreak replicated our synthetic mortality study on a much larger scale. Chapter 4 is focused on quantifying the total biomass standing in these ecosystems on the cusp of significant change. I recognize that quantifying above ground woody biomass (AGB) is a time consuming and error prone process, and scaling field measured allometrics to the landscape using remote sensing carries with it many methodological roadblocks. I decided to start in a juniper savanna, to best understand how the complex growth morphology of J. monosperma and its root crown based allometry could be scaled remotely. The ground based effort determined that driving the universally applied allometry from (Grier et al, 1992) could be accomplished with good accuracy using canopy volume as a predictor. I took this information to the landscape scale, using lidar derived height to create an object based description of the juniper savanna. By using a simplified Monte-Carlo approach, I incorporated the uncertainties in our root collar estimates and the associated allometric AGB predictions into each canopy object, and was able to predict the AGB of each segment with an average standard deviation of 7  15 kg. While I conducted no destructive biomass harvesting to directly validate our absolute AGB estimates, I proposed a simple workflow to drive existing single species allometrics at the landscape scale.

The future of PJ woodlands is unclear. Recent history suggests piñon pine may continue to experience significant reductions in coverage across the region, with still inadequately quantified responses at the regional scale. This dissertation serves to improve the current understanding of how these sensitive biomes can be monitored remotely, from mechanistic descriptions of disturbance detection and response, to improving the modeling approaches used to quantify changes in ecosystem function, and finally the rapid description of above ground carbon stocks.

Chapters 3[1] and 4[2] represent manuscripts currently in preparation for publication. While the chapters are included each as component elements of my singular dissertation, the works are the culmination of collaboration with multiple co-authors and advisors.

[1]Co-authored by Jan U.H. Eitel, Christopher Lippitt, Lee A. Vierling, Urs Schulthess, and Marcy E. Litvak

[2]Co-authored by Amy Neuenschwander and Marcy E. Litvak

# Chapter 2

# Detecting mortality induced structural and functional changes in piñon-juniper woodland using Landsat and RapidEye time series

## 2.1 Introduction

Climatic conditions and disturbance events that cause tree mortality are predicted to become more severe and frequent, resulting in widespread ecological changes at scales ranging from landscapes to regions (Williams et al, 2012; Choat et al, 2012). However, the impacts of disturbance on ecological function are often poorly understood and are therefore seldom included in broad scale models of forest productivity (Liu et al, 2011). For example, feedbacks associated with significant increases in forest mortality across the globe have potentially caused changes in global temperature and precipitation amount and variability, particularly in the past decade (Allen

et al 2010, IPCC2007). Large scale vegetation mortality is likely to cause increased CO2 flux to the atmosphere in the short term and can lead to lasting changes in ecosystem structure (e.g., reductions in canopy leaf area and changes in understory species composition) with long-term (decadal scale) effects on ecosystem carbon and energy balance (Allen et al, 2010; Adams et al, 2010). A mechanistic understanding is necessary to further elucidate how these mortality induced structural changes relate to changes in functional processes such as energy partitioning, vegetation productivity, and carbon sequestration, and to quantify the impact of these mortality events on terrestrial productivity and/or climate at multiple spatial and temporal scales. In the southwestern US, conditions that trigger tree mortality (e.g., low water availability and high temperature) are predicted to become more in the next century resulting in frequent in increasing tree mortality (Williams et al, 2012). Widespread tree mortality quickly alters the physical structure of the ecosystem in terms of both the rapid changes to the woody overstory and the subsequent responses of the understory vegetation caused by changes in light, moisture, and nutrient availability (Rich et al, 2008). One biome that appears to be very sensitive to climate variability in the southwestern US is piñon-pine/juniper (PJ) woodland, which covers over 24 million ha in the region (Figure 1). A severe drought in New Mexico, Colorado, Utah and Arizona from 1999  2002 (Schwalm et al, 2012; Breshears et al, 2005; Williams et al, 2012) caused dramatic structural change to over 1.5 million ha of PJ woodlands due to the abrupt die-off of 40-95% piñon-pine (Pinus edulis) and 2-25% one-seed juniper (Juniperous monosperma) (Breshears et al, 2005; Shaw et al, 2005; Williams et al, 2010). The resulting differential mortality of the overstory in PJ woodlands has had severe and lasting effects on ecosystem structure. Needle fall from the dead piñon began 6-12 months following mortality (Royer et al, 2011), and the biomass of herbaceous understory increased in response to higher light and soil moisture availability (Rich et al, 2008). Following mortality, stand age structure in these biomes shifted towards a mixture of juniper and juvenile (non-reproductive) piñon, lower-

ing the average canopy height and average stem diameter of the system (Clifford et al, 2008). These structural changes may create legacies of functional change with unknown implications for the carbon, water and energy balance of these disturbed woodlands. Given the broad spatial extent of PJ woodlands across the US, coupled with this biomes high sensitivity to climate change induced drought, it is imperative that methods are developed to understand how structural changes in PJ woodlands following mortality events affect the carbon and water balance of this biome. Much research has focused on the use of satellite remote sensing to monitor and quantify changes in forest structure following disturbances such as insect outbreaks and severe drought (e.g., Wulder et al 2006; Coops et al 2009; Kennedy et al 2007; Huang et al 2010; Spruce et al 2010; Huang et al 2012. The majority of this work has examined forest ecosystems characterized by dense vegetation (LAI$>$ 1.5). However, semi-arid biomes are characterized by sparse vegetation (LAI $<$ 1.5) which poses unique challenges to using a multi-temporal approach that detects structural change as anomalous deviations from long-term or short-term seasonal trends (e.g., Huang et al 2010; Kennedy et al 2010. In ecosystems with sparse vegetation, the measured spectral radiance is strongly influenced by the soil background, which confounds the vegetation spectral signal and thus the ability to remotely sense structural changes over time (e.g., a.R. Huete et al 1985; Huete 1988; Eitel et al 2009). To reduce the confounding effects of soil background on remote sensing of vegetation, spectral mixture analysis (SMA) may be used to isolate the vegetation spectral signal from the spectral signal obtained from the soil (Elmore et al, 2000; Asner and Heidebrecht, 2002; Huang et al, 2010; Li et al, 2012). By decomposing a satellite pixel into its components, SMA can provide the fractional cover of both photosynthetic and non-photosynthetic vegetation, as well as the fraction of bare soil and shadow. For example, (Huang et al, 2010) leveraged the spectral resolution of Landsat TM and ETM+ data to characterize the fractional cover of woody and herbaceous vegetation in a semi-arid woodland. However, in order to describe sub-pixel cover SMA relies

on either spectral libraries or ground collected spectra, both of which rely on data that can be sensitive to the temporal and spatial variability of vegetation, rock and soil, as well as the scale at which the spectra were collected (Asner and Heidebrecht, 2002). The challenge of characterizing sparse vegetation in semi-arid systems may be partially overcome by using high (<= 5x5 m) spatial resolution satellite data. This scale of data is helpful in sparsely wooded areas in particular, because it often allows individual tree crowns to be resolved for analysis (**?**). However, relatively little is known about the use of high spatial resolution satellite imagery to monitor and quantify structural changes in semi-arid biomes following disturbance events. Even if high spatial resolution imagery may allow improved monitoring of structural changes in semi-arid ecosystems, relatively little is known about how these structural changes can be linked to changes in ecosystem function, namely changes in gross primary production (GPP). Our overall objective was to examine the potential role of satellite remote sensing towards an improved understanding of mortality induced structural and functional changes in a PJ woodland. Specifically, we tested i) the suitability of satellite time series for monitoring mortality induced structural changes and subsequent changes in ecosystem function in PJ woodlands and ii) how the suitability of satellite remote sensing for monitoring these structural and functional changes is affected by the spatial resolution of the employed satellite imagery. To investigate these questions we used time series of medium (30x30 m; Landsat ETM+) and high spatial resolution (5x5 m; RapidEye) satellite data in concert with GPP data collected in a PJ woodland mortality manipulation experiment near Mountainair, NM.

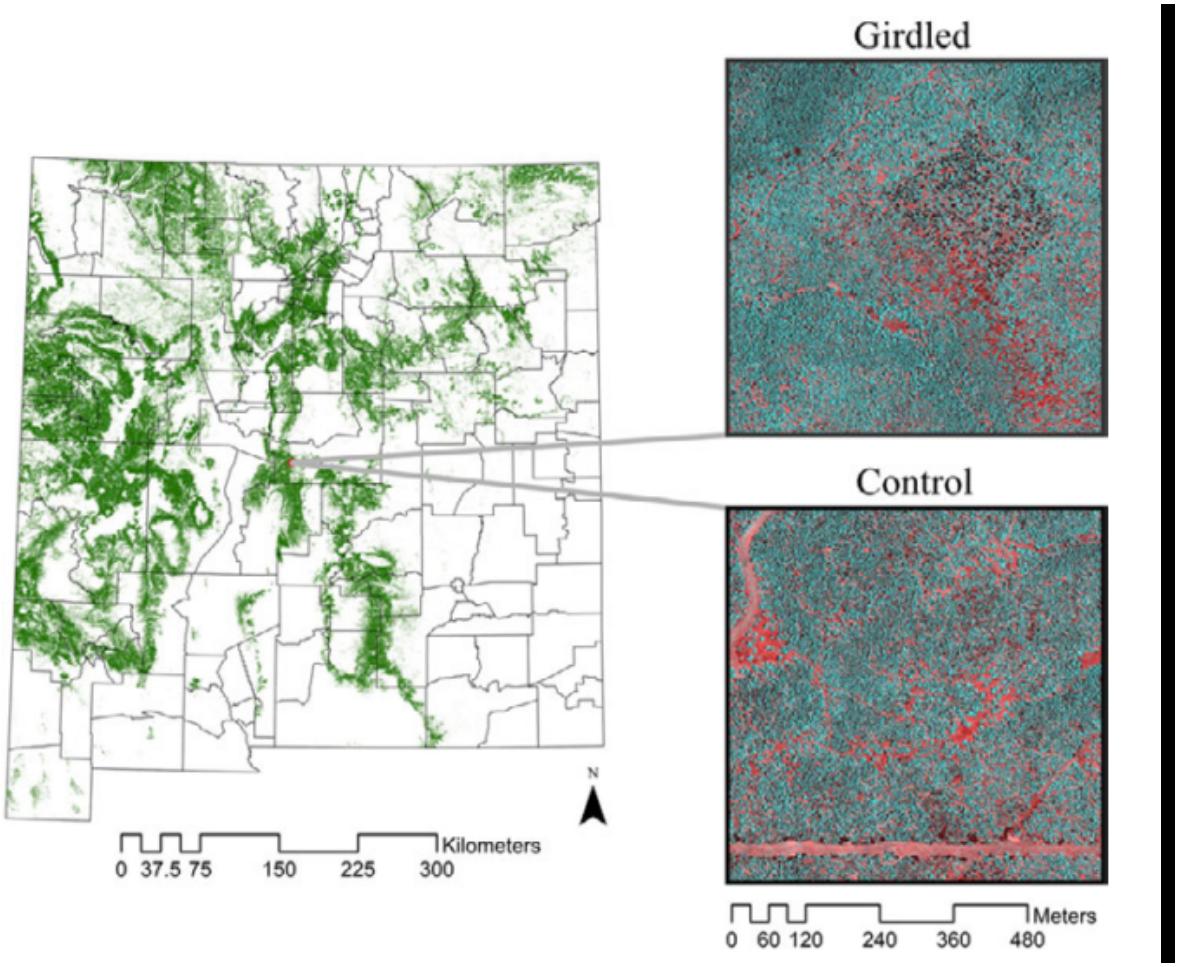


Figure 2.1: The study sites are located < 3 km apart from eachother in central New Mexico. The extent of piñon-juniper woodland across the state is shown in green.

## 2.2 Methods

### 2.2.1 Site Description

The study site includes two piñon-juniper woodlands separated by 3 km and located south of Mountainair, NM (Figure 1). In September of 2009, 1632 adult piñon (>7cm diameter at breast height) in a 4 ha plot in one of the sites (hereafter referred as the

girdled site; 34 26'48.54"N, 106 12'48.63"W) were mechanically girdled by severing the sapwood with a chainsaw at breast height (1.4 m) followed by the application of a 5% glyphosate solution directly applied to the cut to ensure rapid loss of conductivity and subsequent mortality of the trees. The total decoupling of the leaves with the roots following the manipulation was designed to replicate the landscape following the mortality that occurred in the response to the 1999-2002 drought (Breshears et al, 2005; Clifford et al, 2008). The second PJ woodland (hereafter referred to as the control site; 3426'18.420" N, 10614'15.698"W) remained intact. We have continually monitored surface fluxes of carbon, water and energy at each site using tower mounted eddy covariance and associated micrometeorological sensors since 8 months prior to the girdling manipulation in February 2009 (Fox et al., 2013). The soil at both sites is Turkey Springs stony loam, characterized by an abundance of alluvially deposited limestone (Soil Survey Staff). The climate of the region is semi-arid, with a mean annual precipitation of 372mm (+/- 86.8 mm standard deviation, sd) and mean, max, and min temperatures of 19.8C (+/- 0.77C sd) and 2.32C (+/- 0.64C sd) respectively, over the past 20 years (PRISM Climate Group, Oregon StateUniversity, http://prism.oregonstate.edu, created 28 June 2004). Incoming moisture to the site is largely bimodal, broken into winter snow melt from January to March and seasonal monsoon precipitation between August and October with a pronounced dry season occurring from April through July.

### 2.2.2 In situ field measurements

Eddy covariance derived surface fluxes of carbon dioxide, water and energy were measured at 10 Hz using a 3-axis sonic anemometer (CSAT-3, Campbell Scientific, Logan, UT, USA) and an open path infrared gas analyzer (Li-7500, LiCor Biosciences; Lincoln, NE, USA). Data processing of tower fluxes and instrumentation was identical at both sites and described in Fox et al. (2013). Continuous measures

of net radiation, air temperature and relative humidity, soil temperature, photosynthetically active radiation, and soil moisture were made using a CNR1 (Kipp and Zonen, Delft, Netherlands), HMP45C (Vaisala RH probe with aspirated radiation shield Helsinki, Finland), TCAV (averaging thermocouple probes, 27 per site), and up-facing quantum sensors (Li-190SB, Licor Biosciences) respectively. ECHO probes (TE 5cm, Decagon Devices, Pullman, WA, 27 per site) were used for the measurements of volumetric water content (VWC) at each site. The fluxes were aggregated to 30 minute intervals and were corrected for temperature and moisture variations (WPL, Webb et al 1980) as well as frequency responses according to Massman (2000). Anemometer tilt due to terrain variability was corrected using a planar fit method. We used a friction velocity (u*) filter to reject data obtained when turbulence was low (u* less than a threshold value). Data gaps created by the u* filter, malfunctioning instruments, and rain were filled following Lasslop et al (2010). We partitioned the gapfilled net ecosystem exchange (NEE) into the components of total C uptake through photosynthesis or Gross Primary Productivity (GPP), and total carbon leaving the ecosystem through both autotrophic and heterotrophic respiration (Re). We used exponential relationships between nighttime NEE and temperature following the methods of Lasslop et al. (2010) to calculate continuous ecosystem respiration during the day. GPP was then calculated as NEE  Re (Flanagan et al, 2002).

### 2.2.3 Plot level vegetation sampling

In 2008 (before the girdling treatment occurred), the density of annual forbs was recorded in 1 m2 quadrats beneath the canopy and in adjacent interspaces (outside the drip line of any trees) of seven piñon trees at each site. In 2011, four tree and interspace 0.25 m2 quadrats at each site were monitored and permanently marked, and in 2012, those plus an additional five sets were monitored. No density monitoring occurred in 2009 or 2010. Density records for 2011 and 2012 were compared to 2008

data. A generalized linear model using backwards stepwise removal was fit to predict forb density with site, canopy vs. interspace, and the interaction term as predictor variables. Generalized linear models were fit for each year separately. All statistical analyses were run in the open-source statistical software package R 2.14.0 (R Core Team, 2012).

### 2.2.4 Remote sensing image data and pre-processing

We utilized RapidEye imagery and Landsat 7 ETM+ imagery in this study. Time series of 28 RapidEye images (September 2009 to October 2011) and 37 Landsat image dates (January 2009 to December 2012) were obtained to coincide with the girdling experiment. While we radiometrically and geometrically processed the RapidEye data in house, Landsat data were utilized as standardized downloaded products. We obtained RapidEye data (RapidEye AG, Brandenburg, Germany) with top of atmosphere and dark object subtraction (TOA-DOS) having been performed by the vendor following standard procedures (after Collette et al., 1997, Jr. 1988. The imagery has an orthorectified pixel size of 5 x 5 m with 5 spectral bands: blue (440-510 nm), green (520-590 nm), red (630-685 nm), red-edge (690-730 nm), and near-infrared (760-850 nm). We manually georectified each RapidEye image to a master using 50 ground control points per image and second order polynomial transformation and bilinear resampling (RMSE ¡ 0.5 pixels). Then, we radiometrically normalized the RapidEye images using the iterative re-weighted multivariate alteration detection (IR-MAD) algorithm in Python (PythonXY ver. 2.7.3.1) (Nielsen et al, 1998; Canty and Nielsen, 2008). Landsat products were downloaded in standard form for use in this study. Normalized Difference Vegetation Index (NDVI) collected by Landsat ETM+ was downloaded using the Web Enabled Landsat Database (WELD; http://globalmonitoring.sdstate.edu/projects/weld/WELD_ATBD.pdf) (Roy et al, 2010). Spectral vegetation indices were calculated for both regions measured by the

flux towers, both as site-wide area averages ( 200 x 200 meter flux footprints) for Landsat and RapidEye (36 pixels for Landsat, and 1500 pixels for RapidEye) and at the single pixel scale for RapidEye for cover type averages (35 pixels per cover type). At the pixel scale, we used a cover-specific normalized difference between the two sites:

$$VIn = (C - G)/(C + G) \tag{2.1}$$

where VIn is the normalized vegetation index (VI, C is the VI value at the control site, and G is the VI value at the girdle site. The resulting VIn values ranged between -1 to 1. This normalization allowed removal of dynamic patterns in VI that were not caused by the treatment but rather by phenology and soil moisture effects present at both sites (e.g., Eitel et al., 2011)

### 2.2.5 Pixel Extraction

The extent of the tower fetch was described using a flux source area model (Hsieh et al, 2000) that we expanded to two dimensions following Detto et al (2006). After calculating the footprint using long term averages of the model inputs, we georectified the model output with an image from the RapidEye derived time series and defined the tower fetch as all of the pixels falling within the 70th percentile isopleths. To increase the signal of vegetation dynamics in this sparsely vegetated system, RapidEye pixel selection was split into two categories: canopy and interspace. Canopy pixels selected for analysis in the girdled site were dominated by girdled piñon and were chosen using a multi-temporal Normalized Difference Vegetation Index (NDVI) differencing technique. Images of the girdled site prior to the manipulation were subtracted from images later in the time series, in winter, fall and spring. The resulting difference images across all three seasons were used to identify change that only occurred within the tower fetch and that occurred in all three image pairs to account

for seasonal green-up of herbaceous species. An equal number of pixels representing healthy canopy was selected from the control tower fetch using winter NDVI images. Interspace pixels were chosen in an identical manner but representing areas between crowns. Pixel selections at the both the girdle and control site were validated using very high resolution (0.5 meter panchromatic, 2 meter multispectral), co-registered WorldView-2 (DigitalGlobe, Inc., Longmont, CO) derived site maps. We also applied this differencing technique to estimate the percent change in the fractional cover of the woody overstory that occurred at the girdle site following the manipulation, using a NDVI threshold to count pixels that had been defoliated as a result of the treatment.

### 2.2.6 Vegetation Index Selection

Using the RapidEye dataset, we calculated three vegetation indices for our analysis: NDVI, the Normalized Difference Red Edge index (NDRE), and the Modified Soil Adjusted Vegetation Index (MSAVI2). The NDVI (Tucker, 1979) calculated as follows,

$$NDVI = \frac{NIR - RED}{NIR + RED} \tag{2.2}$$

Where NIR is the near-infrared reflectance and RED is the red reflectance. NDVI was used because it is one of the most widely used vegetation index to probe vegetation structure (e.g., LAI) and production (e.g., GPP) (Wang et al, 2005) as well as its sensitivity in sparsely vegetated regions (Yang et al, 2012). Due to the sensitivity of NDVI to soil reflectance in low LAI systems (**?**) such as PJ woodlands, and given the rapidly changing quality of the soil reflectance as a function of precipitation, we also used a second structural index MSAVI2 which is designed to maximize the vegetation signal of systems with low vegetation cover and high, dynamic soil reflectance

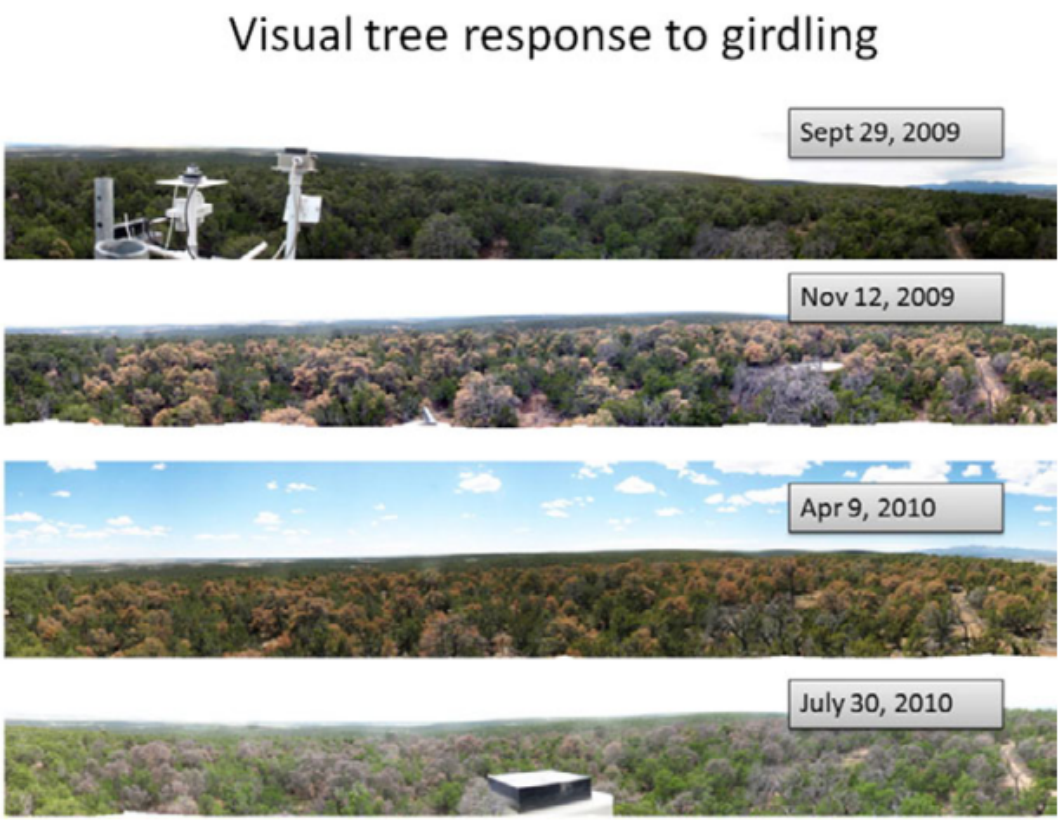


Figure 2.2: A phenocam placed atop the flux tower at the girdled manipulation site provides a timeline of major, visible structural change that took place following the manipulation, from before the manipulation took place (top) to total loss of needles on all manipulated trees (bottom).

(Qi et al, 1994). The MSAVI2 was calculated as follows:

$$MSAVI2 = \frac{(NIR - RED)(1 + L)}{NIR + RED + L} \tag{2.3}$$

Finally, the NDRE was selected because of its sensitivity to both canopy structure and foliar chlorophyll concentration (Gitelson and Merzlyak, 1996; Gitelson et al, 2005; Eitel et al, 2011). The latter might provide additional information when trying to link remotely sensed information to changes in plant function. The NDRE was

calculated as follows:

$$NDRE = \frac{NIR - RED\ EDGE}{NIR + RED\ EDGE} \tag{2.4}$$

where RED EDGE is the reflectance measured in the red-edge region (690-730 nm) of the electromagnetic spectrum. NDVI products for both sites were also collected using Landsat ETM+ as described above.

## 2.3 Results

### 2.3.1 Overstory vegetation structure changes and ecosystem productivity

The selective mortality of the adult piñon in the girdled fetch took place in September of 2009. The canopy quickly became chlorotic, with large decreases in canopy chlorophyll within 22 days following the manipulation (see Eitel et al., 2011). By August 2010 all of the needles from the girdled trees had fallen to the ground (Figure 2). Using ground based measurements and using the allometric relationship in Jenkins et al. (2003), we estimated that approximately 216.5 g C $m^{-2}$ was added to the surface as litter, which decreased LAI by 0.7 m2 $m^{-2}$ or roughly 33%. We validated this estimate from the allometric relationship by comparing the results to the total needle biomass measured from five trees destructively harvested from our site in 2009.

At the ecosystem scale, the high reduction in the systems capacity to take up CO2 following the mortality of the large piñon was evident as a large reduction in GPP relative to the control site. After normalizing the fluxes between the control and girdled sites using pre-girdled fluxes at each site, it is clear that the piñon

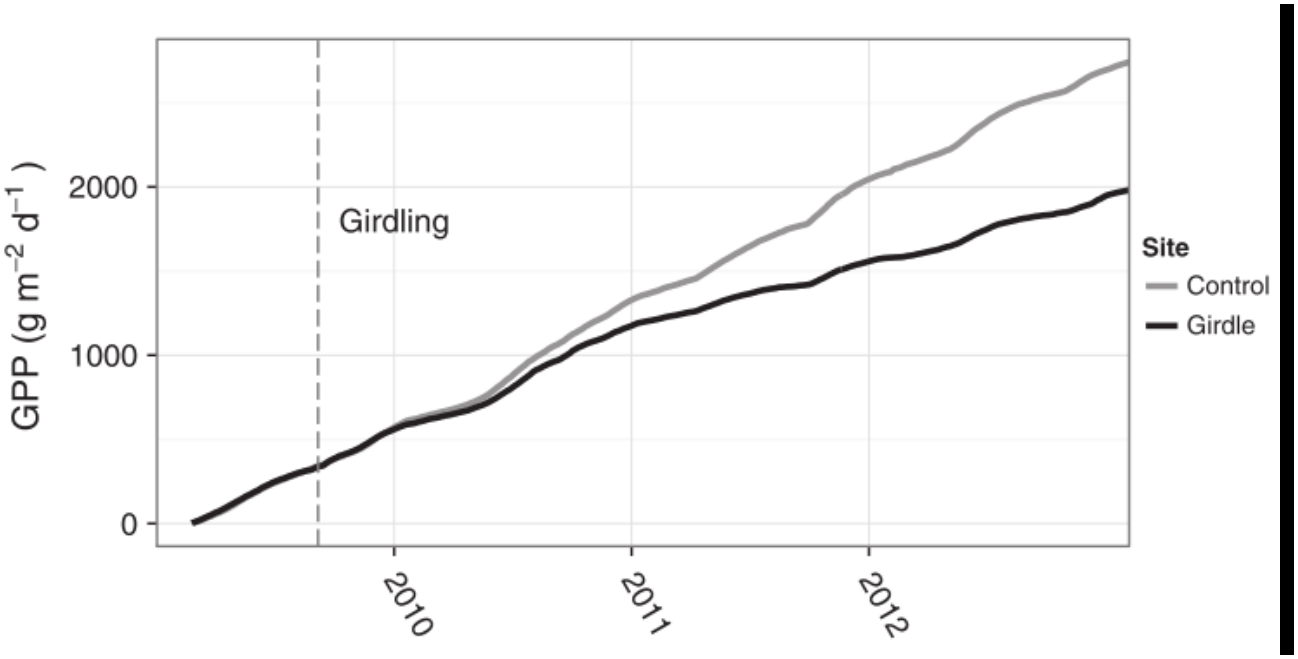


Figure 2.3: Cumulative gross primary productivity throughout the manipulation for both the control (gray) and girdle (black) sites. The time of the girdling is marked with a vertical dashed line.

mortality triggered a cumulative loss of 540 g C m$^{-2}$ taken up by the canopy through photosynthesis in the three years after the girdling (Figure 3), resulting in a 25% decrease in productivity at the girdle site relative to control. Landsat ETM+ and RapidEye were used to remotely sense the disturbance at girdled site (Figure 4). The Landsat ETM+ NDVI (30 x 30 m pixels) begins to decline at the girdled site during the spring of 2010, following the winter snow melt, about 1 year following the disturbance. The canopy pixels monitored by RapidEye (5 x 5 m) show different trends and timing of green-up, with differences in NDVI 30 days following the girdling that persist throughout the time series (Figure. 4c). The RapidEye derived NDVI of the woody overstory decreased by approximately 40% by the end of 2011 (Figure 4c). Following the first year of the disturbance, the girdled site continued to show decreases in VI at multiple scales, most likely due to the secondary mortality of small

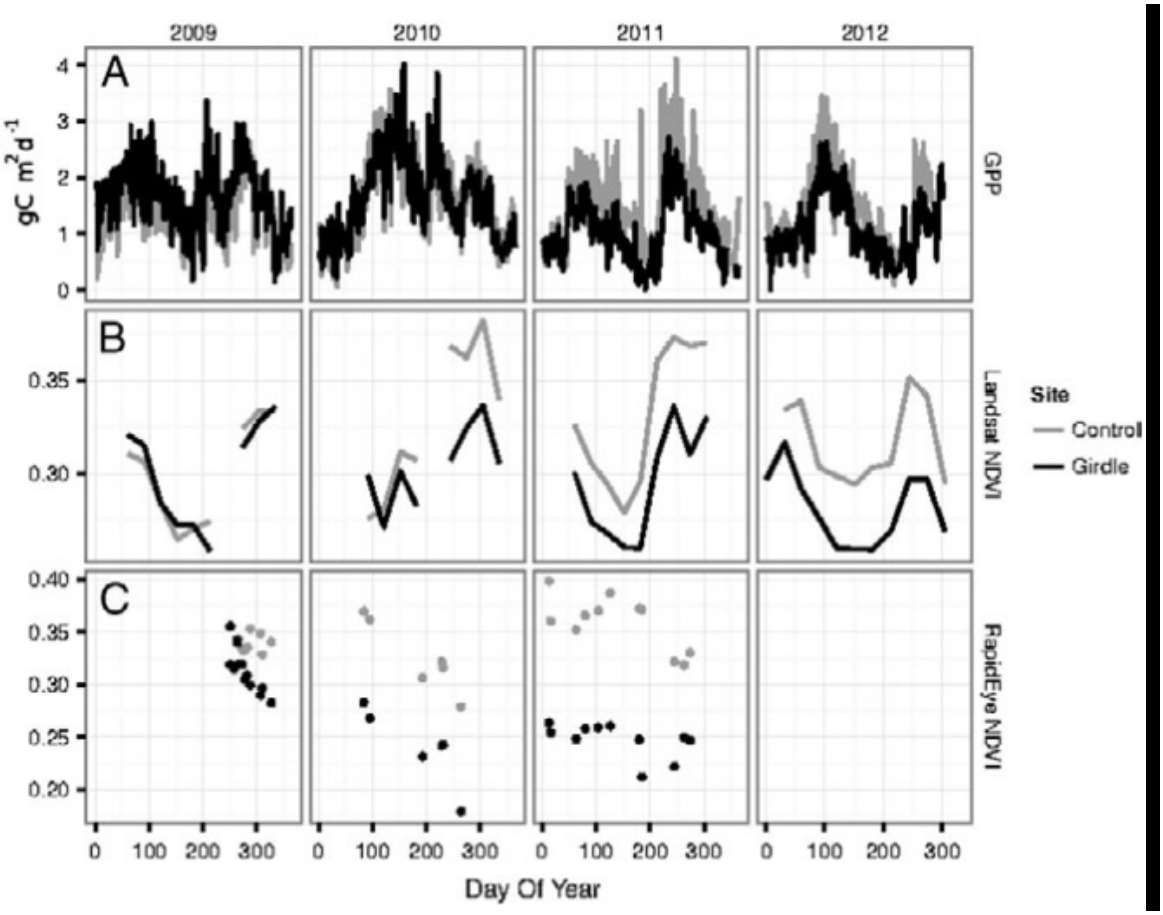


Figure 2.4: Time series of A) gross primary productivity measured at the flux tower, B) Landsat ETM+ derived NDVI, and C) RapidEye NDVI, for both the control (gray) and girdle (black)sites.

piñon.

### 2.3.2 3.2 Understory vegetation structural changes and ecosystem productivity

VI of the girdled crowns began to reverse their trajectories in 2011 from a downward to an upward trend (Figure 5). This change in trajectory of the normalized VI

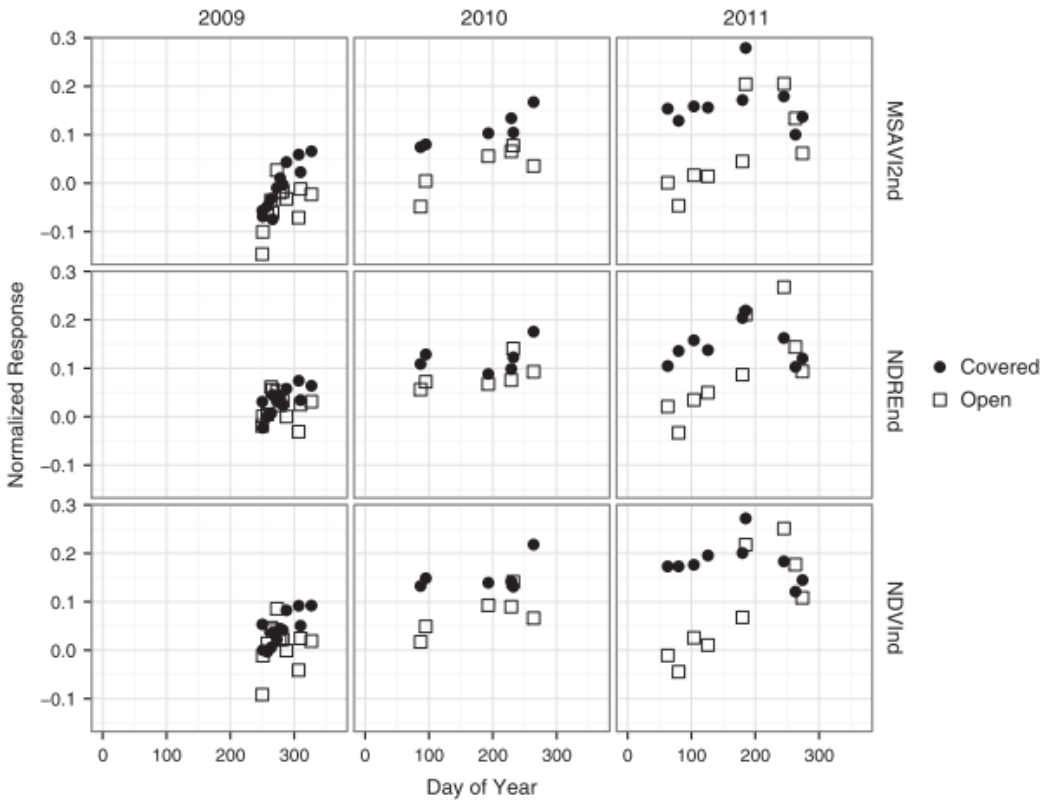


Figure 2.5: RapidEye derived cover specific responses for the girdled trees (closed circles) and the spaces between girdled trees (open squares). The data are normalized relative to the control site: positive values indicate the index is greater at control.

suggests an increase in LAI of the pixels dominated by girdled vegetation, relative to the healthy overstory at the control site. Both NDVI and MSAVI2 mildly reflect this pattern; however, the NDRE shows a strong pattern of senescence and subsequent green-up, potentially indicating the growth of low LAI, high chlorophyll vegetation. The strong pattern exhibited by the NDRE to these changes might be explained by the high sensitivity of NDRE to both canopy structural properties and foliar biochemistry (e.g., Gitelson and Merzlyak 1994, Gitelson and Vina 2005; Eitel et al., 2011). Ground level analysis of the sites following the manipulation support this observation and show that the underlying cause of this green-up is the significantly

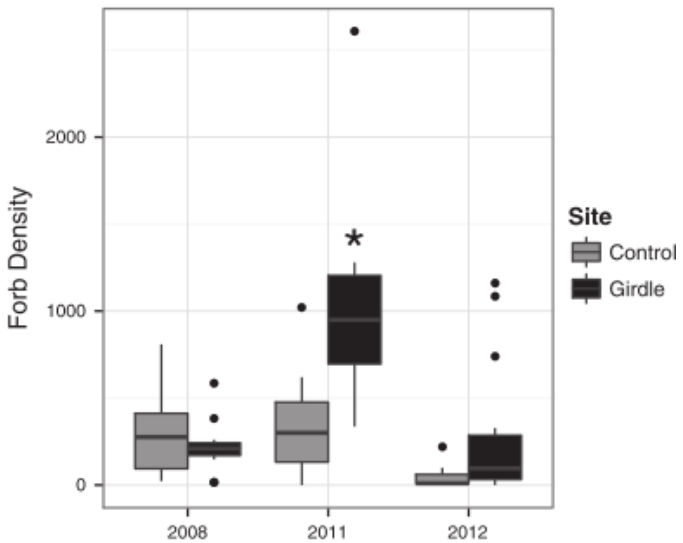


Figure 2.6: Forb density before and following the manipulation at both the control (gray) and girdle (black) sites. Outliers are plotted as points, and are defined as values which are 1.5 times greater than the 75th percentile. Significance $^*P < 0.001$ is marked by an asterisk.

($P < 0.05$) higher establishment of annual forbs at the girdle site relative to the control site (Figure 6).

There were significant ($P < 0.05$) site effects in 2011 and 2012 but the interactions between canopy and interspace were not statistically significant ($P > 0.05$). Furthermore, forb cover increased at the girdled site relative to control site, but we did not measure a statistically significant trend in the change in the relative cover of grasses or CAM functional types following the manipulation. The positive relationship between VWC and site averaged NDVI appeared to be influenced by this shift in understory structure as well, given the larger sensitivity on soil moisture to green-up at the girdled site, with an $R^2$ for NDVI of 0.21 at the control site compared to 0.84 at the girdle site (Figure 7). Both sites exhibit much weaker relationships during drought conditions (Figure 8).

The trends of the VI for interspace pixels suggest that the overstory manipulation

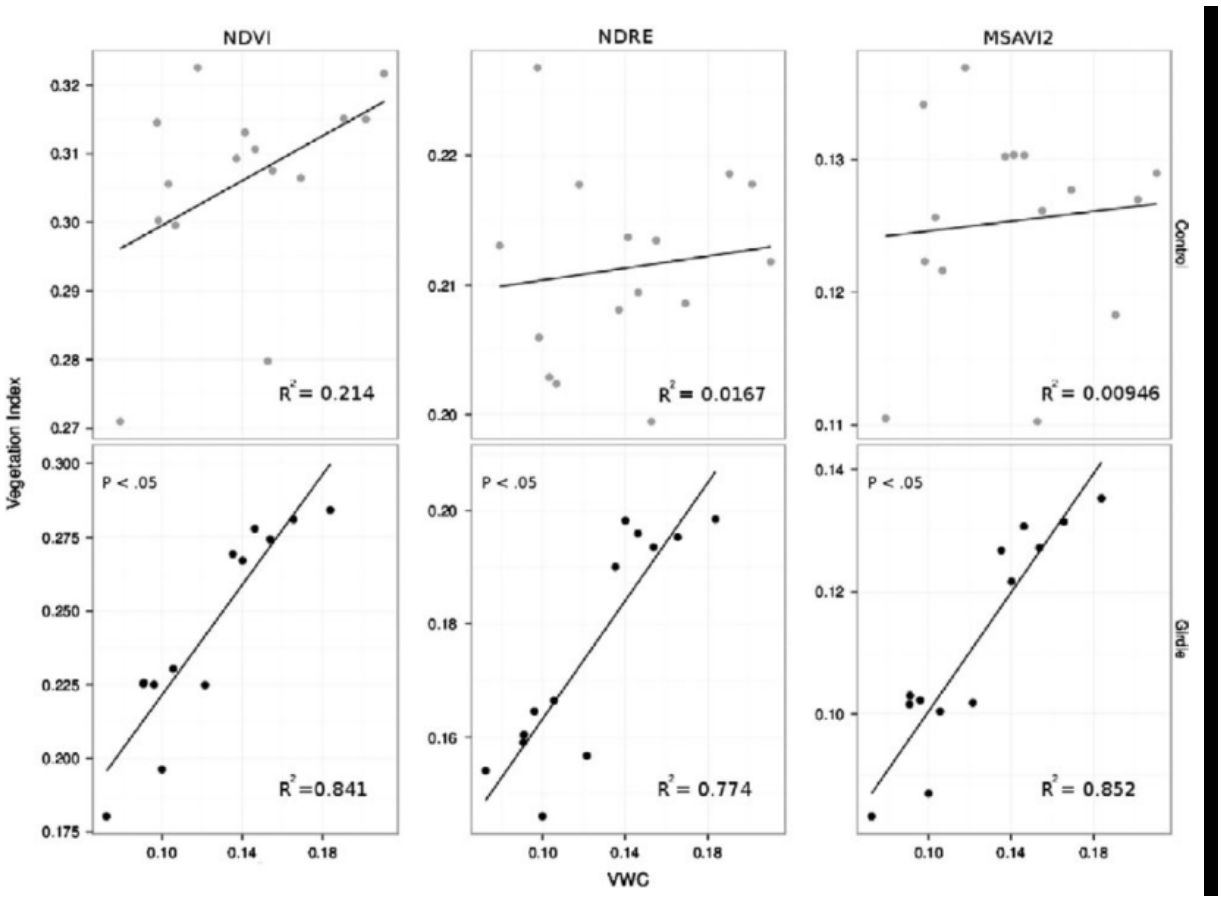


Figure 2.7: Fetch-wide relationship between canopy vegetation indices and soil volumetric water content during periods where temperature and soil moisture are least limiting plant productivity (air temperature > 0C or soilmoisture < 9%).

altered the understory in the region between the canopy cover in a very different way (Figure 5). Over the course of each year the interspace vegetation at the girdle site decreased in both LAI and chlorophyll (as quantified by VI), suggesting the senescence of seasonal grasses and forbs. This is consistent with what we know of the function of these sites which capitalize on winter precipitation and monsoon precipitation, with a dry season in-between. However, the relative difference of the interspace vegetation for the girdle site compared to the control site indicates a differential senescence of the interspace vegetation at the girdle site (Figure 5). This

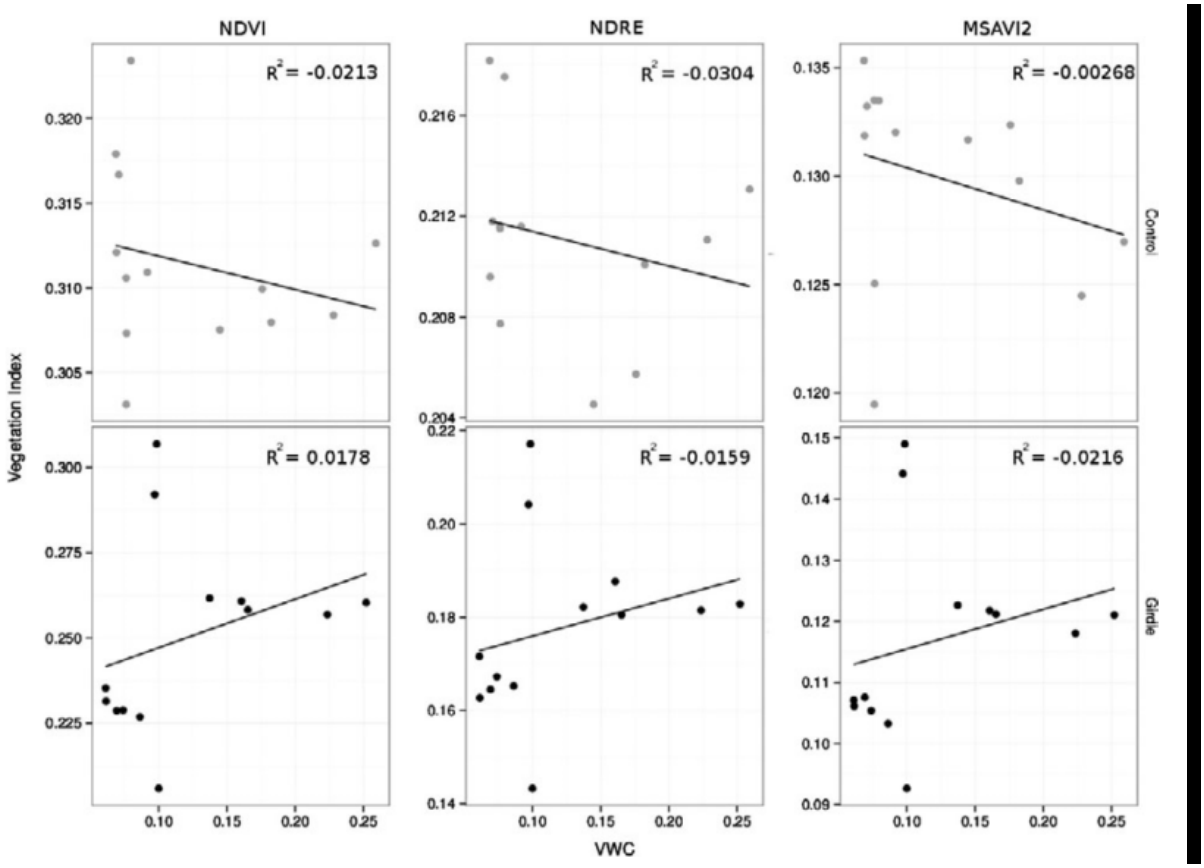


Figure 2.8: Fetch-wide relationship between canopy vegetation indices and soil volumetric water content during periods where temperature and soil moisture are most limiting plant productivity (air temperature $<$ 0C or soilmoisture $<$ 9%).

secondary effect suggests that the decrease in overstory vegetation has affected the longevity of the shallow rooting herbaceous vegetation in-between the canopy crowns. The year to year return to a consistent LAI and chlorophyll content of these interspace regions also indicates that this shift in the function of the interspace vegetation has not altered the initial winter moisture driven green-up that starts the herbaceous cycle each year, but rather has altered the ability of these plants to utilize monsoon precipitation.

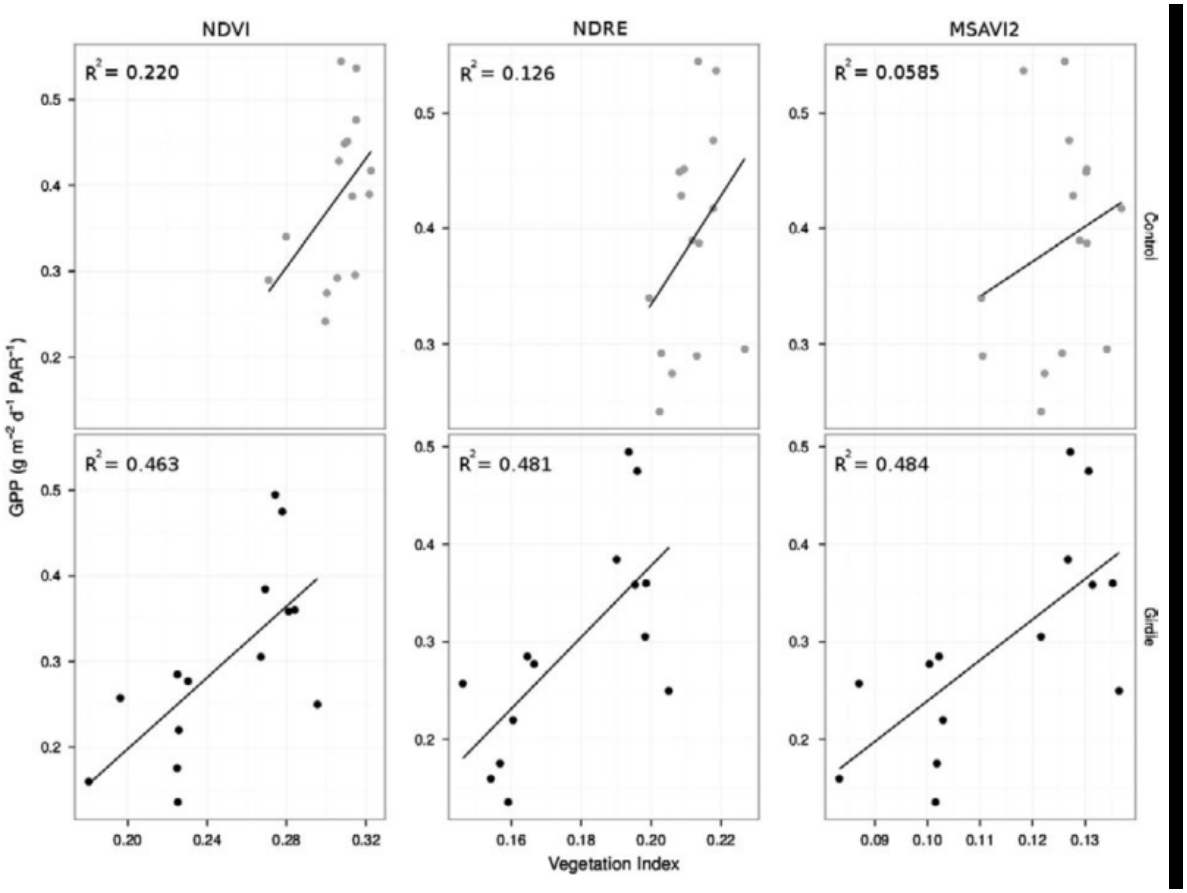


Figure 2.9: Fetch-wide relationship between gross primary productivity and canopy vegetation indices during periods where temperature and soil moisture are least limiting plant productivity (air temperature > 0C or soilmoisture > 9%).

### 2.3.3 Uncoupling of canopy reflectance and ecosystem function

Periods when soil water content is less limiting show a much stronger linear relationship between GPP and VI (Figures 9 and 10) at the girdle site ($R^2 = 0.46$, $P < .05$) compared to the drought periods ($R^2 = 0.13$, $P > .05$.). The control site also shows a decoupling between GPP and VI, but to a lesser degree ($R^2 = 0.22$, $P <.05$ during growing conditions, compared to $R^2 = 0.09$, $P > .05$ during drought conditions).

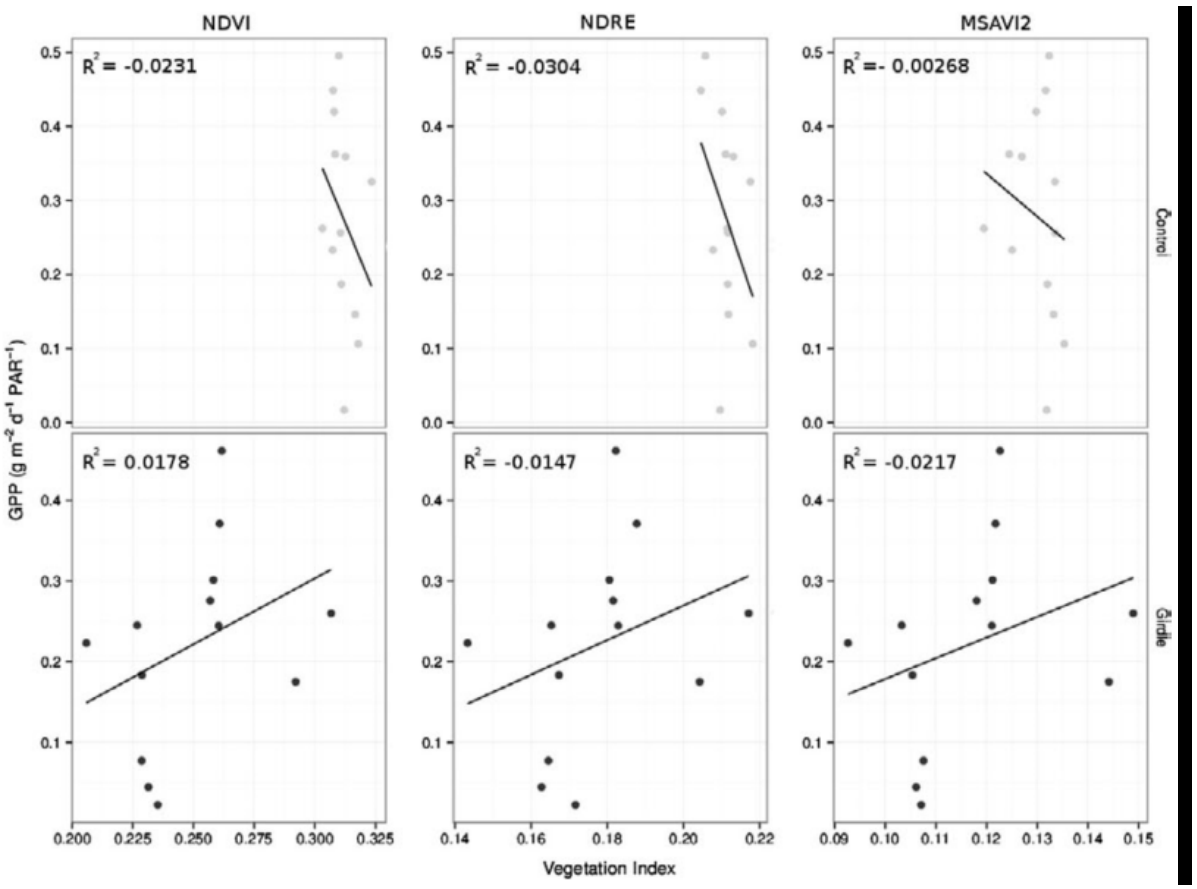


Figure 2.10: Fetch-wide relationship between gross primary productivity and canopy vegetation indices during periods where temperature and soil moisture are most limiting plant productivity (air temperature $<$ 0C or soilmoisture $<$ 9%).

Both of the sites are severely water limited, with the dominant control over GPP being soil moisture (Figure 10). The rate at which the girdled site greens up with increases in soil water is now much greater relative to the control site (Figures 7 and 8). The amount of green-up that occurs at the girdled site also has had a significant influence on the relationship between the VI and GPP, showing a greater initial slope relative to the control site. This suggests that the increase in understory vegetation has helped offset the uncoupled nature of the VI at the girdled site with GPP.

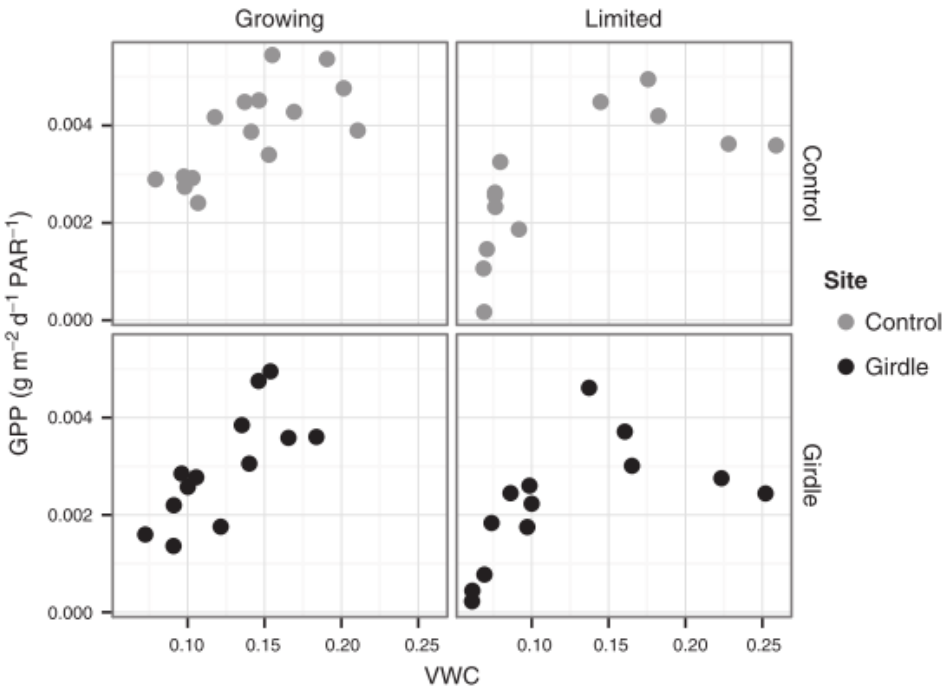


Figure 2.11: Fetch-wide relationship between gross primary productivity and soil water content during growing (temperature > 0C or soil mousture > 9%) and growth limited (air temperature < 0C or soilmoisture < 9%) conditions.

## 2.4 Discussion

### 2.4.1 Utility of time series imagery for canopy structural change detection

Our manipulation severely altered the structure of the ecosystem causing a variety of cascading effects on ecosystem function such as changes in phenology and the timing and magnitude of carbon uptake. This case study allowed us to characterize how well high spatial resolution (5x5 m) RapidEye imagery could be used to detect and characterize changes in canopy structure that followed as a result of the manipulation relative to coarser resolution Landsat ETM+ (30 x 30 m). The initial mortality

of the adult piñon at the girdle site resulted in a significant loss of leaf area, leaving the girdled fetch comprised of primarily juniper and non-reproductive piñon which is the normal species assemblage that typically survived following the severe regional drought and bark beetle outbreak of 1999-2002 (Clifford et al., 2008). Our girdling manipulation caused sudden drops in chlorophyll content just days following the disturbance (see Eitel et al., 2011) as opposed to weeks following the disturbance onset typically seen in taller, less arid coniferous canopies (Edburg et al, 2012). By the end of 2010, the girdled crowns were fully chlorotic (Figure 2) and by the end of 2011 field allometric measurements suggested a loss of 33% of the leaf area at the girdled fetch. The initial decline in foliar chlorophyll concentration seen before the end of 2009 was not reflected by Landsat ETM+ NDVI, most likely due to the coarser spatial resolution (30 x 30 meter pixels) of the sensor being affected by the healthy juniper and small piñon crowns. The higher resolution RapidEye data (5 x 5 meter) show a much faster response, with all three VI reflecting the initial canopy stress. During this period, the RapidEye NDRE exhibited the highest sensitivity to the disturbance (see Eitel et al., 2011) and NDVI reflected the largest drop in canopy reflectance by the end of 2009. Landsat ETM+ lagged in detecting the response relative to RapidEye by about 1 year. When the canopy became fully chlorotic in 2010, RapidEye and Landsat ETM+ both detected large differences. In the final year of the experiment, the Landsat ETM+ and RapidEye trends remain, as NDVI from both platforms continues to decline reflecting the mortality of the some of the remaining juniper or small piñon within the girdled tower fetch. The first year that large structural changes begin to occur in the understory of the girdled piñon is 2011, as detected from RapidEye via NDVI and MSAVI2 (Figure 5) when low LAI vegetation established under the girdled piñon crowns. This shift in understory structure, however, does not appear to alter cumulative GPP at the girdle site, suggesting the establishment of forbs is not yet significant enough to alter GPP at the girdle site. In the long term, the increase in understory green-up may preclude the detection of the

disturbance in the region, ultimately reducing the ability of remote sensing driven models of terrestrial carbon capture to accurately track post-mortality dynamics in these ecosystems (Huang et al, 2010). Our combined approach of structural analysis and in-situ carbon balance measurements may help circumvent these issues in the future, by allowing the structure-specific parameterization of remotely driven models of GPP. The increase in herbaceous plants beneath the dead piñon trees at the girdle site may explain the large difference in the green-up response to soil moisture, relative to the control site. Figures 7 and 8 highlight the uncoupled nature between the VI and soil water content at the control site ($R^2$ decreasing from 0.22 to 0.09 under low soil moisture conditions), contrasting with the stronger relationship at the girdle site ($R^2$ decreasing from 0.46 to 0.13 under low soil moisture conditions). The shallow rooting, herbaceous understory vegetation in this system was likely benefiting from increased needle deposition which can reduce nutrient, light and moisture competition (Breshears and Barnes, 1999) and facilitate leaf out.

### 2.4.2 Higher spatial resolution imagery aids semi-arid canopy change detection

Previous work in quantifying carbon stock losses in PJ woodlands (Huang et al, 2009, 2010, 2012) has leveraged high resolution aerial imagery coupled with moderate resolution (30 m) satellite time series and spectral un-mixing techniques to establish a relationship between the fraction of woody cover and biomass. The major advantage of this approach is the ability to scale estimates of NPP to the region and landscape. Within a single Landsat ETM+ pixel, the spectral mixing approach can provide a fraction of woody to herbaceous cover, yet the specific relationship of where the herbaceous components are greening or senescing relative to the overstory cannot be ascertained. These spatially distributed relationships between overstory and understory structure are critical to understand in order to predict how disturbance will

alter the function in semi-arid woodlands. The five meter spatial resolution of the RapidEye sensor and the temporal density of our time series allowed us to track individual clumps of crowns over time, and determine that the herbaceous establishment observed under the girdled piñon was not present between the girdled crowns. As a result, we now are establishing a mechanistic understanding of how these secondary understory structural changes are influencing ecosystem carbon balance, a yet uninvestigated topic which may have a significant impact at the regional and landscape scales. This cover specific response of the understory to overstory disturbance has been documented in other semi-arid regions and is consistent with the way these systems use light and water (Breshears and Barnes 1999, Breshears et al., 1997, Rich et al., 2008), but to our knowledge has yet to be characterized remotely and understanding this effect on ecosystem scale changes in function is requisite for the development of structure-function linked ecosystem models.

### 2.4.3 Monitoring the function of semi-arid biomes using satellite imagery hinges on water availability

Though the RapidEye derived indices performed well at tracking the structural changes in the ecosystem (reduction in canopy LAI, increase in the herbaceous green-up), the relationship between canopy reflectance and ecological function of the canopy was highly decoupled. Thus, linking remotely characterized changes in ecosystem structure with tower-measured GPP requires a more nuanced analysis, for example by using spectral information that has been shown to be sensitive to light use efficiency (Gamon et al, 1992, 1997). Given the semi-arid nature of PJ woodlands, as with all water limited systems, carbon uptake is generally governed by the presence of water (Figure 11, Huxman et al 2004; Muldavin et al 2008), which is stochastic and ephemeral. The uncoupling is essentially due to the fact that on most days, plant stomata have fully closed by late morning to resist desiccation, as

vapor pressure deficit rises into the afternoon. Evergreen canopies typically respond to pulses of water by adjusting stomatal conductance and the rhizosphere, rather than up-regulating chlorophyll production or leaf area which is typically observed in herbaceous and deciduous vegetation (Huxman et al., 2004). Consequently, integrated measures of CO2 uptake recorded by the tower show varying relationships with spectral VI such as NDRE, NDVI, and MSAVI2 that are sensitive to changes in chlorophyll content and LAI. By using our ground based measures of VWC, we can select only those days where soil water (and air temperature) were not limiting. This dramatically increases the strength of the linear relationship between the VI and GPP (Figure 7), yet this relies on ground based estimates of soil water content. National soil moisture monitoring networks (e.g., the NRCS snowpack telemetry network) or the recent development of GPS based soil moisture monitoring (Larson et al, 2008) may potentially provide some of the required soil moisture data to parameterize future models of GPP in these sparse, semi-arid systems. The dependence of the VI on soil moisture reflects the moisture limitations in these systems. Furthermore, this dependence suggests the utility of the VI to monitor canopy status or predict GPP is contingent on there being sufficient moisture in the soil to allow photosynthesis to take place.

## 2.5 Conclusions

This case study focused on determining the potential role of satellite remote sensing in developing a more mechanistic understanding of the structural changes that take place in piñon juniper woodlands following disturbance events and how those structural changes affect the function of the ecosystem. We determined that both moderate (Landsat ETM+, 30 x 30 meter pixel size) and high (RapidEye, 5 x 5 meter pixel size) resolution satellite remote sensing platforms generally are capable

of temporally resolving structural changes in Piñon-Juniper woodlands (PJ) following disturbance events. However, the complexity of the structure of PJ woodlands creates a highly heterogeneous mixture of live and dead vegetation, dense and sparse overstory, and the presence or absence of herbaceous constituents. This complex nature of PJ woodlands is what drives many researchers to leverage the spectral differences between those various ecosystem components by employing techniques such as spectral mixing analysis. This approach has worked well for determining the fraction of photosynthetic or non-photosynthetic woody vegetation, herbaceous cover, or bare soil in a moderately sized pixel (e.g., 30 x 30 m from Landsat TM or ETM+), yet the spatial relationship between the change in cover or function of these various constituents limits the ability to create a mechanistic understanding of the structural changes (e.g., how changes in the overstory relate to changes in the understory). To circumvent this challenge we utilized high spatial resolution data and determined that the structural response of the ecosystem following disturbance indeed has a spatial component. Specifically, the herbaceous ramp-up that occurred post-mortality was limited to the region below the crowns of dead trees. Further, the regions between the dead crowns showed almost the opposite result, suggesting the change in energy balance of the ecosystem following the loss of the canopy reduced the ability of the herbaceous layer to establish in crown interspaces after the disturbance. The impact of these structural changes on the function of the ecosystem was difficult to remotely determine. Initially, the loss of canopy following the disturbance was readily tracked by remote sensing platforms at multiple spatial scales, with high spatial resolution data (5 x 5 m) allowing detection almost a full year earlier. However, relating remote sensing data of the disturbance event and the subsequent recovery of the herbaceous layer with the in-situ measures of ecosystem productivity measured by flux towers yielded poor relationships. Our data suggest that this phenomenon is due to the uncoupling of the reflectance of the ecosystem with the function of the ecosystem during periods of drought, which for PJ woodlands can

represent a large portion of the year. Consequently, we conclude that the inclusion of high spatial resolution satellite time series can aid in developing mechanistic models of recovery from disturbance in these heterogeneous systems, but future work should focus on ways to improve our ability to predict canopy function even during periods of drought which pervade this widespread and sensitive southwestern biome.

# Chapter 3

# Remote sensing based simple models of GPP in both disturbed and undisturbed piñon-Juniper woodlands in the Southwestern U.S.

## 3.1 Introduction

Semi-arid regions and drylands together cover 41 - 46% of the globe. In spite of the low fractional cover of vegetation and minimal annual precipitation, the contribution of semi-arid biomes to the global uptake of carbon dioxide from the atmosphere can be significant on annual time scales (Poulter et al., 2014). The inter-annual variability of precipitation in these ecosystems can result in both rapid carbon stock accumulation, and then subsequent turnover due to frequent disturbance (e.g., drought,

insect outbreak, fire), but these relationships on the net storage of carbon are poorly understood (Poulter et al., 2014). The climate in the southwestern United States (US) has recently experienced both increased regional air temperature, and decreased precipitation, both of which are projected to increase in the coming decades (Seager et al 2007, 2012, IPCC2007, IPCC2014, National Climate Assessment, 2014). The combined effects of these changes in climate have increased drought severity, exacerbated ecosystem stress, and ultimately triggered widespread forest mortality across the region (Allen et al, 2010; Clifford et al, 2013). Given the rapid state transitions of vegetation in these climatically sensitive biomes, and the projected changes in climate and associated mortality for this region (Williams et al, 2012), accurate monitoring of carbon uptake dynamics in these semi-arid ecosystems is an essential part of constraining uncertainties associated with regional carbon balance. Monitoring ecosystem carbon uptake over large geographic extents requires the use of remote sensing. Typically, remote sensing driven models of ecosystem function predict Gross Primary Productivity (GPP), the total atmospheric carbon taken up via photosynthesis (e.g., Running et al (1999); Zhao et al (2011). Satellite remote sensing provides the means to predict GPP by employing light use efficiency-based algorithms (Monteith, 1972; Monteith and Moss, 1977) that rely on vegetation indices (VIs) such as the normalized difference vegetation index (NDVI, Tucker (1979)). This approach has been used at a variety of sites and scales, both by employing empirical (e.g., Sims et al (2008, 2014)) and light use efficiency / process driven techniques (e.g., Yuan et al (2010)), generally using high temporal resolution, coarse spatial resolution ( >= 250 meters) remote sensing data from sensors such as the Moderate Resolution Imaging Spectrometer (MODIS) (e.g., Running et al., 1999). In most biomes, the basis of remotely sensed GPP estimation hinges on quantifying relationships between changes in abiotic drivers (namely photosynthetically active radiation (PAR), and air temperature) and concomitant changes in canopy biochemical (e.g., foliar chlorophyll, nitrogen, and water concentration), and/or biophysical

(e.g., leaf area index (LAI)) properties which are typically captured well by NDVI (e.g. Mynenni et al., 2005). However, in semi-arid regions, vegetation function is constrained by water availability for the majority of the year, with periods of drought and heat interrupted briefly by spring snow melt or episodic pulses of precipitation. Consequently, in these biomes, changes in NDVI are constrained primarily by the availability of water, rather than light or temperature, (Fensholt et al, 2012). This results in canopy VIs and GPP often being decoupled in semi-arid regions due to low soil moisture, particularly where evergreen plants are present (Krofcheck et al., 2014). Other characteristics unique to semi-arid ecosystems that challenge the use of NDVI for characterizing changes in GPP in these biomes are highly variable precipitation which trigger high interannual variability in GPP due to water seasonal water limitations, but low variability in LAI and/or chlorophyll concentration (subsequently low variability in NDVI). Further, the low LAI ($< 1.5$ mean LAI across landscapes) and spatially heterogeneous plant canopies typical of these systems can result in further uncertainties due to high reflectance by the soil background, thus confou nding spectral signals relating to plant function (e.g., Huete et al., 1985, Huete et al., 1988, Eitel et al 2009). Here we test the ability of spectral VIs other than NDVI to model GPP in semi-arid ecosystems. We focus particularly on piñon-juniper woodlands for several reasons. First because it is the largest biome in the Southwestern US covering 18 million ha in NM, AZ, CO and UT. Second, the changes in climate in this region have triggered a significant amount of mortality in this biome (Clifford et al, 2008, 2013), and thus, quantifying the extent of this disturbance on productivity throughout the region is crucial to understanding how this extensive mortality has impacted both current and future carbon dynamics. Finally, we take advantage of an existing experimental manipulation in a PJ woodland in central NM that was girdled in 2009 to simulate the widespread piñon mortality observed throughout the region. The advantage of using this experimental manipulation is that since the girdling in 2009, changes in ecosystem productivity triggered by this mortality have been continuously

monitored using eddy covariance since, and compared to similar measurements in a nearby intact PJ woodland that serves as a control. Recent research (e.g., Eitel et al., 2011) over this experimental manipulation suggested that the red-edge employing normalized difference red-edge index (NDRE) (**?**) was more sensitive than NDVI to the observed decrease in leaf chlorophyll concentration triggered by piñon girdling in this PJ woodland. The increased sensitivity of NDRE over NDVI was also more effective in detecting increases in greenup of the low LAI herbaceous vegetation following mortality in this same system (Krofcheck et al., 2014). The first hypothesis we tested was that the observed variability in NDRE will allow us to more accurately estimate GPP in both the disturbed and undisturbed PJ woodland in this experimental manipulation. Secondly, due to the inherent dependence of productivity on water availability in this biome, we tested if adding the normalized difference wetness index (NDWI) (**?**), a VI that is sensitive to changes in foliar water content significantly improved the model fit, by constraining the model error during periods of low canopy water content. Finally, given the highly heterogeneous nature of PJ woodlands, we tested the hypothesis that VI generated from higher spatial resolution (5 meter) data would provide more accurate estimates of GPP relative to traditional, moderate resolution (30 meter) remote sensing data.

## 3.2 Methodology

### 3.2.1 Site Description

The study site includes two piñon-juniper woodlands separated by 3 km and located south of Mountainair, NM. In September of 2009, 1632 adult piñon (¿7cm diameter at breast height) in a 4 ha plot in one of the sites (hereafter referred as the girdled site; 3426'48.54"N, 10612'48.63"W) were mechanically girdled by severing the sap-

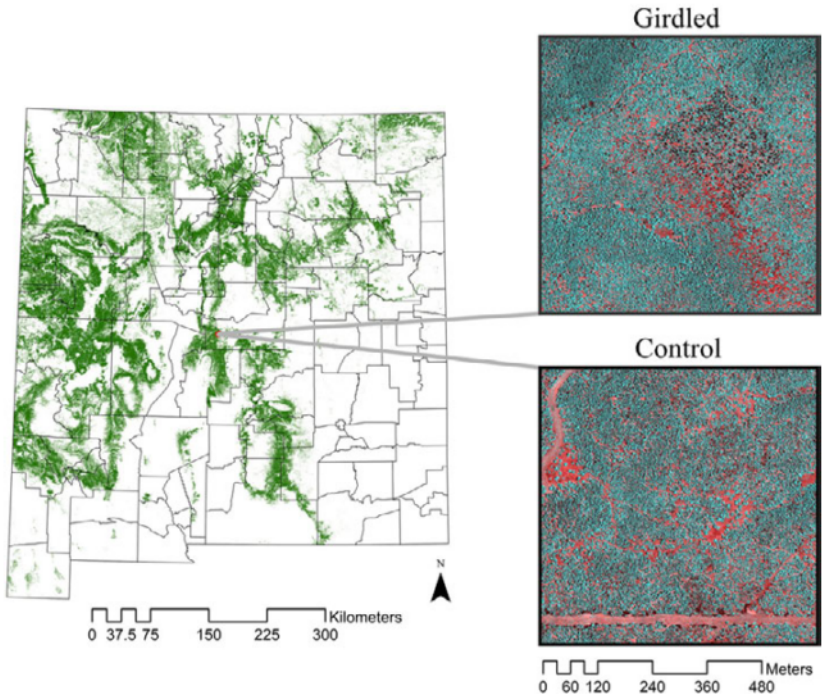


Figure 3.1: The study sites are located < 3 km apart from eachother in central New Mexico. The extent of piñon-juniper woodland across the state is shown in green.

wood with a chainsaw at breast height (1.4 m) followed by the application of a 5% glyphosate solution directly applied to the cut to ensure rapid loss of conductivity and subsequent mortality of the trees. The total decoupling of the leaves with the roots following the manipulation was designed to replicate the landscape following the mortality that occurred in the response to the 1999-2002 drought (Breshears et al., 2005, Clifford et al., 2008). The second PJ woodland (hereafter referred to as the control site; 3426'18.420" N, 10614'15.698"W) remained intact. We have continually monitored surface fluxes of carbon, water and energy at each site using tower mounted eddy covariance and associated micrometeorological sensors since 8 months prior to the girdling manipulation in February 2009. The soil at both sites is Turkey Springs stony loam, characterized by an abundance of alluvially deposited limestone (Soil Survey Staff). The climate of the region is semi-arid, with a mean

annual precipitation of 372mm (+/- 86.8 mm standard deviation, sd) and mean, max, and min temperatures of 19.8C (+/- 0.77C sd) and 2.32C (+/- 0.64C sd) respectively, over the past 20 years (PRISM Climate Group, Oregon StateUniversity, http://prism.oregonstate.edu, created 28 June 2004). Incoming moisture to the site is largely bimodal, broken into winter snow melt from January to March and seasonal monsoon precipitation between August and October with a pronounced dry season occurring from April through July.

### 3.2.2 Data: gross primary productivity

Data processing and instrumentation is identical at both sites. Eddy covariance (EC) derived surface fluxes of carbon, water and energy were measured at 10hz using a 3-axis sonic anemometer (CSAT-3, Campbell Scientific) and an open-path infrared gas analyzer (Li-7500, LiCor Biosciences; Lincoln, NE, USA). Additionally, continuous measures of net radiation, air temperature and relative humidity, soil temperature, photosynthetically active radiation, and soil moisture (volumetric water content) were made using a CNR1 (Kipp and Zonen, City, Country), HMP45C (Vaisala RH probe with aspirated radiation shield City Country), TCAV (averaging thermocouple probes, 27 per site), up facing quantum sensors (Li-190SB, Licor Biosciences) and ECHO probes (TE 5cm, Decagon Devices, Pullman, WA, 27 per site) respectively. The fluxes were aggregated to 30 minute intervals and were corrected for temperature and moisture variations (WPL, Webb et al., 1980) as well as frequency responses according to Massman (2000). Anemometer tilt due to terrain variability was corrected using a planar fit method. We used a friction velocity (u*) filter to reject data obtained when turbulence is low (u* less than a threshold value). Data gaps created by the u* filter, malfunctioning instruments, and rain were filled following Lasslop et al. (2010). We partitioned the gapfilled net ecosystem exchange (NEE) into the components of total C uptake through photosynthesis (i.e., GPP)

and total carbon leaving the ecosystem through both autotrophic and heterotrophic respiration (Re). We used exponential relationships between nighttime NEE and temperature following the methods of Lasslop et al., (2010) to calculate continuous ecosystem respiration during the day. GPP was then calculated as NEE  Re (Flanagan et al, 2002). We used a flux source area model (Hsieh 2000) modified for 2 dimensions by Detto et al., 2002, to characterize the experimental region at both sites that are measured by the flux towers. The source area model suggested that the four hectare analysis region at each site accounted for approximately 80% recovery at the tower level. In this way we ensured that the remote sensing data and the EC measurements were representing the same patch of vegetation.

### 3.2.3 Data: Landsat ETM+

We used the web enabled Landsat database (WELD) web service (Roy et al., 2010) to download time series of Landsat ETM+ data from 2009 to 2011 for 36 pixels within the four hectare area measured by each flux tower. Each pixel time series was cleaned using the QA/QC data associated with WELD products (Roy et al., 2010), only the pixels classified as containing no saturated bands and not cloudy (determined by the automatic cloud cover assessment algorithm, ACCA) (Irish et al., 2006), were retained. To remove effects of snow cover on the VI, the normalized difference snow index (NDSI) was used to remove snow covered pixels from the analysis. If more than 25% of the total analysis region for either the control or girdled site was covered by snow, the entire acquisition date was removed from the analysis. Snowy pixels were characterized as having an NDSI $> 0.2$. The majority (82 %) of the Landsat ETM+ data were acquired $<= 3$ days of a RapidEye acquisition (see section 2.2.3), with the greatest time separation being 10 days. The cleaned Landsat ETM+ pixel time series were linearly interpolated to daily intervals for comparison with the RapidEye data. In this manner, the same number of Landsat ETM+ VI and RapidEye VI

were used in each of the models tested. Geolocation error for the Landsat ETM+ imagery was generally $< 0.5$ pixel according to the WELD documentation.

### 3.2.4 Data: RapidEye

A time series of 46 images (September 2009 to October 2011) were delivered with a top of atmosphere, dark object subtraction (TOA-DOS) correction applied by RapidEye, Inc (now BlackBridge Ltd of Alberta, Canada). We manually co-registered each image to a master (September 2009) using 50 ground control points and a second order polynomial transformation. 15 - 20 check points per image resulted in each scene being co-registered to an of RMSE $< 2.5$ m (ERDAS Imagine 2010). Eighteen images were excluded from the time series due to snow or cloud cover. Existing site boundary shapefiles were used to clip the images to the extent of both the control and girdled sites, coincident with the pixels extracted for the Landsat ETM+ analysis (Python Software Foundation. Python Language Reference, version 2.7. Available at http://www.python.org)

### 3.2.5 Spectral vegetation indices

NDVI, NDRE, and NDWI were calculated to inform our simple models of GPP and to test our hypotheses. NDRE and NDWI are only available using RapidEye and Landsat ETM+ respectively however, indicated by their subscripts in the Table 1. The red edge here refers to a waveband on the RapidEye constellation of sensors that spans 690 to 730 nm.

$$NDVI = \frac{NIR - RED}{NIR + RED} \tag{3.1}$$

$$NDRE = \frac{RED - RedEdge}{RED + RedEdge} \tag{3.2}$$

$$NDWI = \frac{NIR - SWIR}{NIR + SWIR} \tag{3.3}$$

### 3.2.6 Statistical analysis

We fitted six multiple linear regression models in R 3.0.1 (R Development Core Team, 2013). Each regression model is structured as follows: GPP  PAR x TA x VI (4)

where PAR is photosynthetic active radiation, TA is air temperature, and VI depicts one or more vegetation index that are shown in table 1. GPP, PAR, and TA were derived from on-site instrumentation (for GPP, see section 2.2.1). The spatial resolution of the resulting model parameters was either 5 meters (from RapidEye), 30 meters (from Landsat ETM+), or a combination in the case of the mixed models.

Table 1. VI inputs for the model framework. Each of the three greenness VI options was tested with and without the inclusion of NDWI, resulting in six simple models. Each model is structured as GPP  PAR x TA x VI where VI is represented by the corresponding table entry above, while PAR and TA are derived from on-site instrumentation.

Within each model group, we created a hierarchical structure of models containing all possible combinations of parameters and one first order interaction term. In this way we aimed to compare model groups by comparing the models with the best set of parameters within each group. Model performance was characterized using both the adjusted $R^2$ ($R^2$adj) and the adjusted Akaike information criterion (AICadj) both of which add an additional penalty for increasing model complexity.

$$R^2_{adj} = 1 - \frac{1 - R^2 * (n-1)}{n - k - 1} \tag{3.4}$$

$$AIC_{adj} = AIC + \frac{2k * (k+1)}{n - k - 1} \tag{3.5}$$

Where k = the number of parameters and n = the number of observations. We chose the AICadj as a second performance index due to the relatively small number of observations and to avoid model over fitting (**?**). The best combination of parameters within each model group hereafter, chosen by the largest AICadj weight, and largest relative log likelihood, a measure of how likely a given model is actually the best choice, was selected at the control and the girdle site separately.

## 3.3 Results and Discussion

### 3.3.1 Models of GPP in PJ woodlands had the lowest error at the disturbed site

Data driven, simple linear models driven by PAR, air temperature, and remotely sensed vegetation indices (VI), we were able to explain up to roughly 80% of the variability of GPP in both intact, and disturbed PJ woodlands, however the strength of this relationship was contingent on a tight coupling between the variability in VI and canopy function. The best performing model VI at the undisturbed PJ woodland was Landsat ETM+ derived NDVI (normalized difference vegetation index), whereas at the disturbed site the red-edge VI performed best ($R^2$adj of 0.81 and 0.84 respectively).

Consistent with previous work by Krofcheck et al., 2014, the coupling between VI and canopy function therefore may be significantly influenced by both the interannual variability in climate, and ecosystem disturbance regimes. This is evident in both the control and girdled sites in 2009 (Figure 3). At the control site, the Fall of 2009 was very productive, with a strong monsoon bringing sufficient moisture to the ecosystem, and consequently the coupling of Landsat ETM+ NDVI, PAR, and air temperature explained roughly 80% of the variability seen in GPP. In the case of

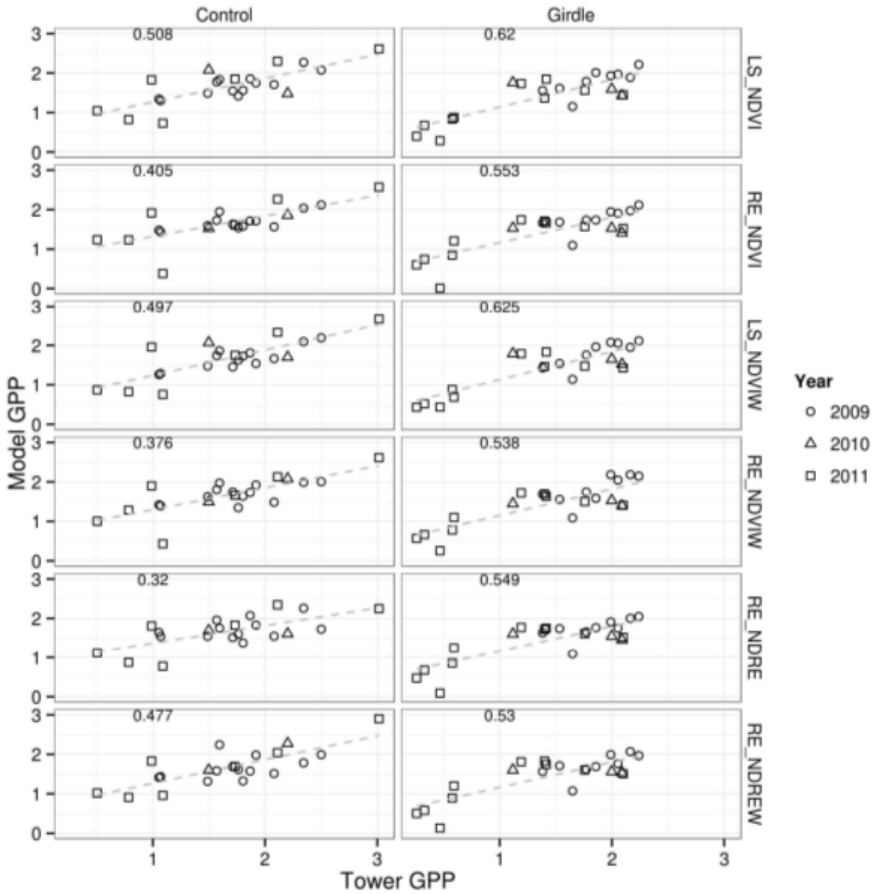


Figure 3.2: Linear model fit 1:1 curves for all model forms in the hierarchy. Data for the control and girdle sites are fit independently (left and right columns respectively). LS and RE denote Landsat and RapidEye.

girdled site during the same period, the manipulation in piñon mortality drove both the rapid decrease in VI, and the sudden decrease in canopy uptake of carbon. Both during this period of significant canopy stress, and throughout the entire analysis period, the best model fits were seen at the girdled site, possible due to the increased coupling between the VI and GPP, previously documented as a potential effect of the manipulation itself (Krofcheck et al., 2014).

| | *Control* | | | *Girdle* | | |
|---|---|---|---|---|---|---|
| | $\delta AIC$ | $RelativeLL$ | $R^2_{adj}$ | $\delta AIC$ | $RelativeLL$ | $R^2_{adj}$ |
| Landsat ETM+ | | | | | | |
| $NDVI_{LS}$ | 0.00 | 1.00 | 0.63 | 1.37 | 0.50 | 0.52 |
| $NDVI_{LSw}$ | 0.095 | 0.62 | 0.66 | 4.20 | 0.12 | 0.57 |
| RapidEye | | | | | | |
| $NDVI_{RE}$ | 18.43 | 0.00 | 0.06 | 8.77 | 0.01 | 0.29 |
| $NDRE_{RE}$ | 16.82 | 0.00 | 0.13 | 3.63 | 0.16 | 0.46 |
| $NDVI_{REw}$ | 2.83 | 0.24 | 0.67 | 7.65 | 0.02 | 0.58 |
| $NDRE_{REw}$ | 9.28 | 0.01 | 0.44 | 0.00 | 1.00 | 0.61 |

Table 3.1: Adjusted AIC and adjusted R2 fit statistics for all model forms in the hierarchy, parameterized using the entire data set, from the Fall of 2009 to the Winter of 2011.

### 3.3.2 NDRE and NDWI reduced model error only during periods of significant stress

When we drove the model hierarchy with data from all three years in the study, the simplest Landsat ETM+ NDVI based models performed best ( $R^2$adj = 0.51 at control, $R^2$adj= 0.62 at girdle). The fit statistics from the both the Landsat ETM+ and RapidEye driven models improved significantly when a single year (2009) was used to drive the regression (Figure 3), dramatically increasing the fit of the simple Landsat ETM+ NDVI model at the control site ($R^2$adj from 0.51 to 0.81) and increased the fit of the RapidEye NDRE and NDWI model at the girdled site ( $R^2$adj from 0.53 to 0.84). During this period, there was a tight coupling between VI and canopy funciton at both the control site due to ideal growth conditions, and the girdled site, due to the imposed piñon mortality.

In our linear model hierarchy, GPP predictive models which only use RapidEye

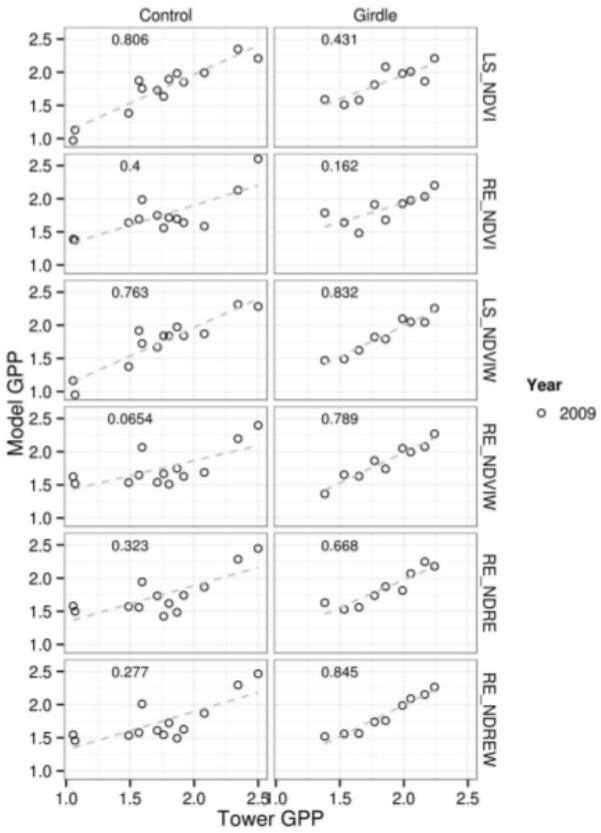


Figure 3.3: Linear model fit 1:1 curves for all model forms in the hierarchy, parameterized with only data from 2009. Data for the control and girdle sites are fit independently (left and right columns respectively). LS and RE denote Landsat and RapidEye.

NDVI showed no significant improvement in model performance when compared to the inclusion of NDRE (Figure 2, table 2). Previous work in this region suggests NDRE is more responsive to decreases in canopy chlorophyll concentration relative to NDVI, yet following a lag period (roughly 2 weeks), the NDVI performs equally well in quantifying foliar concentration of chlorophyll (Eitel et al., 2011). Given that our time series spans multiple years, with rapid decreases in canopy chlorophyll occurring only at the girdled site in 2009, we ran the same model structures on only data from 2009, which captured the girdling process (Figure 3). Over this smaller time period

| | *Control* | | | *Girdle* | | |
|---|---|---|---|---|---|---|
| | $\delta AIC$ | $RelativeLL$ | $R^2_{adj}$ | $\delta AIC$ | $RelativeLL$ | $R^2_{adj}$ |
| Landsat ETM+ | | | | | | |
| $NDVI_{LS}$ | 0.00 | 1.00 | 0.63 | 1.37 | 0.50 | 0.52 |
| $NDVI_{LSw}$ | 0.095 | 0.62 | 0.66 | 4.20 | 0.12 | 0.57 |
| RapidEye | | | | | | |
| $NDVI_{RE}$ | 18.43 | 0.00 | 0.06 | 8.77 | 0.01 | 0.29 |
| $NDRE_{RE}$ | 16.82 | 0.00 | 0.13 | 3.63 | 0.16 | 0.46 |
| $NDVI_{REw}$ | 2.83 | 0.24 | 0.67 | 7.65 | 0.02 | 0.58 |
| $NDRE_{REw}$ | 9.28 | 0.01 | 0.44 | 0.00 | 1.00 | 0.61 |

Table 3.2: Adjusted AIC and adjusted R2 fit statistics for all model forms in the hierarchy, parameterized using only data from 2009

of significant canopy stress, the NDRE dramatically improved model performance at the girdled site ($R^2$adj from 0.16 for NDVI to 0.67 for NDRE, Table 3). However, no improvement in NDRE driven model fit was seen at the control site, which is consistent with the idea that NDRE explains variability in canopy function best during periods of rapid canopy change. The incorporation of Landsat ETM+-derived NDWI into the model structure did not improve model fit in either Landsat ETM+ or RapidEye based models when the entire time series was used in the regression (Figure 2, table 2). NDWI did however dramatically reduce prediction error in both Landsat ETM+ and RapidEye based models at the girdled site, in 2009 alone (Figure 3, table 3). Previous work has also shown that the inclusion of a Landsat ETM+ moisture index has improved estimates of productivity in dryland ecosystems (e.g., (Leuning et al, 2005), in spite of the finding that the NDWI may be less effective in sparse canopy systems Gu et al., 2008. However, in semi-arid coniferous woodlands, our data suggest the NDWI may only improve estimates of productivity during rapid changes in canopy status, such as canopy mortality. Moisture sensitive VI have also

been shown to be less effective at representing canopy water content during periods of low to moderate drought stress (Rock et al, 1986; Eitel et al, 2006), suggesting that GPP predictions during periods of the year when water is less limiting may not benefit from the inclusion of a canopy moisture VI as much as during periods of drought stress.

### 3.3.3 Inconsistency in sensor view imposed significant variability RapidEye VI model performance

Our hypothesis that VI generated from higher spatial resolution data should be a better predictor of ecosystem carbon uptake, according to the fit statistics in Table 2, was not proven with models parameterized using the entire analysis period. However, we expected that the null hypothesis in this case would be that increased spatial resolution data conferred no improvement over moderate resolution data, rather than a detriment to model performance, as is seen in our results. However, the variability in sensor view angle from scene to scene of higher resolution, pointable sensors, is often inconsistent and in the case of our time series, influenced the apparent fractional cover of vegetation (Figure 4a). In an effort to test whether or not the variability in view angle was imposing noise into the RapidEye data, we chose to bin the analysis by sensor view angles ¿ +/-7.0 degrees, given the majority of our data were collected at more than 7 degrees off nadir (60%, Figure 4b). The resultant fit statistics for the reduced angle model runs are summarized in table 4 (Figure 5). The constrain on absolute sensor view angle significantly improved model fits in RapidEye models driven by NDVI ($R^2$adj increased from 0.40 to 0.73 at the control site, and from 0.55 to 0.70 at the girdled site), in spite of the fact that the resulting view angle constrained data set spanned multiple years, and consequently was describing a large amount of interannual variability (see section 3.1).

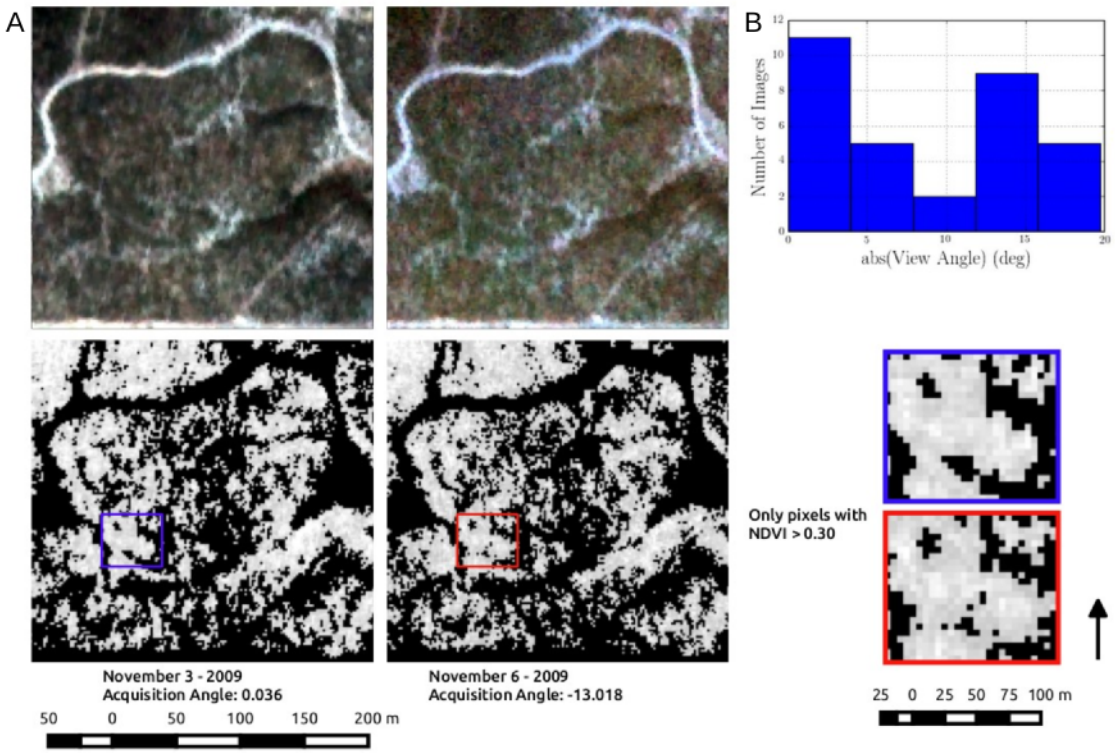


Figure 3.4: (A) RapidEye false color composites of the PJ control site (top), and the corresponding fraction of pixels with NDVI ¿ 0.30 (bottom), with detailed subsets on the far right. (B) Histogram of view angles that comprised the entire RapidEye time series. View angles are represented as absolute values from nadir.

Previous work has shown the effects of sensor view angle on the fractional cover of various feature types (e.g., Stoms et al 1997, pertaining to AVHRR composites), and generally near-nadir view angles are a selection criteria for multi-image or multi-sensor analyses (Abuzar et al, 2014). Given the increasing amount and complexity of remote sensing data at the disposal of terrestrial scientists, multi-resolution and time series data assimilation approaches to developing temporally and spatially resolved remote sensing products will need to address the confounding effects of vegetation cover on sensor angle, especially in sparse canopy systems.

| | *Control* | | | *Girdle* | | |
|---|---|---|---|---|---|---|
| | $\delta AIC$ | $RelativeLL$ | $R^2_{adj}$ | $\delta AIC$ | $RelativeLL$ | $R^2_{adj}$ |
| Landsat ETM+ | | | | | | |
| $NDVI_{LS}$ | 10.22 | 0.01 | 0.66 | 1.71 | 0.43 | 0.42 |
| $NDVI_{LSw}$ | 16.76 | 0.00 | 0.66 | 7.42 | 0.02 | 0.38 |
| RapidEye | | | | | | |
| $NDVI_{RE}$ | 0.00 | 1.00 | 0.70 | 0.00 | 1.00 | 0.73 |
| $NDRE_{RE}$ | 5.25 | 0.07 | 0.59 | 4.16 | 0.12 | 0.60 |
| $NDVI_{REw}$ | 9.30 | 0.01 | 0.69 | 6.43 | 0.04 | 0.65 |
| $NDRE_{REw}$ | 10.86 | 0.00 | 0.59 | 9.18 | 0.00 | 0.61 |

Table 3.3: Adjusted AIC and adjusted R2 fit statistics for all model forms in the hierarchy, parameterized using only data corresponding to dates on which RapidEye images were acquired at view angles <= +/- 7 degrees from nadir.

### 3.3.4 Implications for regional remote sensing based estimations of GPP in PJ woodlands

The results of our case study suggest that remote sensing driven, simple linear models of GPP have the potential to accurately describe patterns in regional carbon uptake, using locally measured PAR and air temperature as covariates. In this study, we chose to use Landsat ETM+ data, given its ease of access via the WELD portal. The highly heterogeneous composition of PJ woodlands, and the small scale of our manipulation experiment (200 x 200 meters), precluded the use of MODIS sized pixels (>= 250 x 250 meters), and given the heterogeneous patterns of mortality and subsequent recovery typical of disturbed PJ woodlands (e.g., Breshears et al., 1997, Clifford et al., 2008, Krofcheck et al., 2014), Landsat scale or finer resolution (<= 30 meters) products are of the appropriate spatial scale to resolve the patchy, heterogeneous patterns of mortality typical in disturbed PJ woodlands. Our hypothesis that

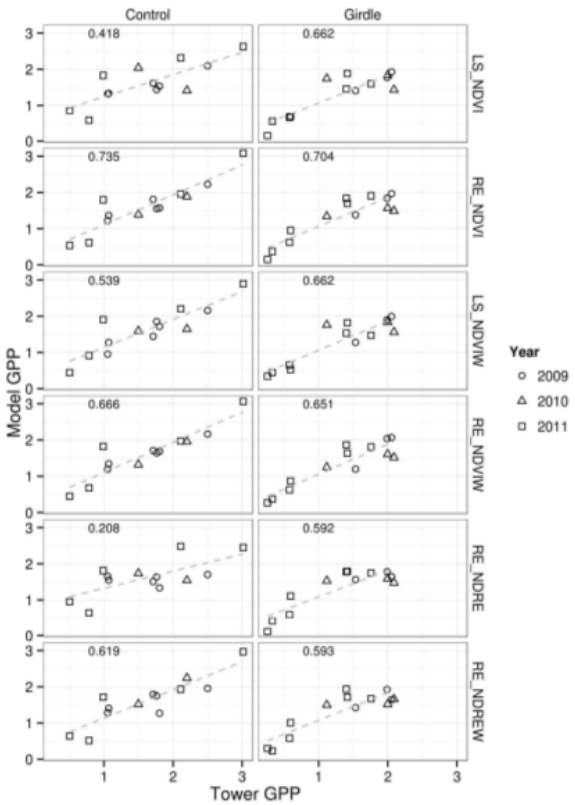


Figure 3.5: Linear model fit 1:1 curves for all model forms in the hierarchy, parameterized with only data corresponding to dates on which RapidEye imagesvwere acquired at view angles <= +/- 7 degrees from nadir. Data for the control and girdle sites are fit independently (left and right columns respectively). LS and RE denote Landsat and RapidEye.

increased spatial scale should improve predictive power of simple models of GPP was difficult to assess in this case, due to noise imposed on the RapidEye data set as a function of sensor angle (see section 3.3). However, limiting image acquisition angle variability dramatically improved model performance, even relative to Landsat ETM+ data, suggesting that increased spatial resolution data may have a role in constraining GPP predictions in these heterogeneous woodlands in the future. The inclusion of the red-edge leveraging NDRE from RapidEye only improved model performance during periods of significant stress, such as during the selective mortality

of piñon pine that we imposed on the girdled site in the Fall of 2009 (see section 3.2). Given the imminent transition in climate projected for the southwestern US, and the already evident impacts on piñon mortality regionally, GPP prediction efforts in PJ woodlands should stand to benefit from the incorporation of NDRE during mortality. Given the upcoming launch of Sentinel-2, which can leverage the red-edge and infra red wavebands required to compute NDRE and NDWI respectively, the potential to incorporate NDRE into near-future regional models of GPP as a consequence of piñon mortality may significantly constrain the current uncertainty associated with piñon mortality and PJ woodland ecosystem function. Further, while NDWI did not significantly contribute to model performance in this study, the measured productivity of semi-arid plant canopies is strongly a function of available water, which ultimately affects the coupling between canopy VI and GPP (e.g., Krofcheck et al, 2014), and consequently the predictive power of VI driven models of GPP in these regions. Remotely sensed regional estimates of surface soil water content from the soon to launch Soil Moisture Active Passive sensor (SMAP), may provide an alternative to constrain the interannual variability in the VI GPP relationship in semi-arid PJ woodlands.

### 3.3.5 Conclusions

Our first hypothesis was based on the previous work with NDRE in PJ woodlands, which showed that NDRE both tracked disturbance caused changes in leaf chlorophyll faster than NDVI (Eitel et al, 2011) and vegetation structural changes in the understory following the disturbance as a result of herbaceous regrowth (Krofcheck et al., 2014). Building on this, we tested whether or not these factors translated to improving simple linear models of GPP. Our findings suggest that while structurally sensitive, NDVI is more informative to models of GPP than NDRE except during periods of extreme stress or disturbance. Given the previously established moisture

limitation in these systems, and the strong relationship between soil moisture and the coupling of VI and GPP, we tested the hypothesis that NDWI would improve estimates of GPP in PJ woodlands. Similarly to our finding related to NDRE, we only saw a significant improvement in model performance using NDWI at the girdling site, during the manipulation event that took place in the Fall of 2009. Finally, the increased spatial resolution of the RapidEye data did improve estimates of GPP in both the control and girdled sites relative to Landsat ETM+, however this was only true when we reduced the variability in scene to scene sensor view angle in our RapidEye time series. While this may not play a strong role in more homogeneous, closed canopy systems, sensor view angle in this study often imposed more variability on NDVI than natural seasonal variability. As a consequence, we recommend that remote sensing efforts to model VI sensitive processes in heterogeneous, low fractional cover systems, place high constraints on acquisition angles for time series, or bin analyses by viewing angle to minimize the potential confounding effects. We recognize that the temporally resolved RapidEye data set we utilized for this study is not a common commodity and currently carries with it a large cost. Therefore we recognize the potential ability of the red-edge data to improve estimates of GPP especially during periods of ecosystem stress, but caution that the improvement may not yet be worth the added complexity incurred by sensor and illumination geometry. However, for questions pertaining to areas of rapid disturbance or recovery where LAI may be changing slowly in relation to chlorophyll content, or for studies specifically aimed at capturing extremes of ecosystem function, our results suggests the use of this or other high resolution, red-edge employing platforms to maximize accuracy during periods of interest. The upcoming Sentinel-2 satellite missions will potentially fill this role, allowing greater spatial and temporal resolution than Landsat, as well as the ability to calculate NDRE and NDWI. Secondly, the upcoming soil moisture active passive sensor (SMAP) may provide either direct measurements, or modeled estimates of soil moisture, providing further predictive power of the carbon

uptake rates in semi-arid ecosystems.

# Chapter 4

# Woody biomass estimation in a Southwestern US juniper savanna using clumped tree segmentation and existing allometries.

## 4.1 Introduction

Semi-arid regions globally are characterized by low above ground biomass (AGB) and low fractional cover of vegetation, with high intra and inter-annual variability in rainfall, resulting in high inter-annual variability in carbon uptake. In spite of the pervasive water limitations in these regions, these ecosystems have been shown to contribute significantly to the global carbon sink when precipitation is high (Poulter et al, 2014). Given the extent of these biomes, quantifying the total carbon stored in them, and the relationship between structural properties and functional processes is crucial to understanding regional carbon dynamics. This requires the ability to

rapidly and accurately assess structural properties such as above ground biomass (AGB) at the ecosystem and landscape scales. Making accurate descriptions of AGB across a wide range of vegetation types and large geographic area extends a critical component to global and national scale climate change mitigation strategies such as REDD+ (Reduced Emissions from Deforestation and Forest Degradation; Gibbs et al 2007). Further, the majority of process based modeling approaches to estimate terrestrial carbon flux require AGB as an input variable, thus the accurate estimations of AGB constrains model error in carbon balance prediction. Conventionally, this process involves allometric relationships that use individual tree canopy shape and stem diameter to predict biomass measurements developed from destructive harvests to generate predictive models of tree biomass across a wide range of species (e.g., (Jenkins et al, 2003; Chojnacky et al, 2013)). Using ground-based measurements to quantify individual tree canopy shape and stem diameter works well to estimate stand biomass at the plot and local scales, yet is often cost prohibitive and logistically challenging to use on large spatial scales (Colgan et al (2013)). Remote sensing of terrestrial vegetation has reduced many of the challenges associated with spatially scaling the estimation of carbon stocks in woody ecosystems. Passive optical approaches from MODIS and Landsat which are considered coarse (>= 30 meter) resolution sensors have historically been used to regress vegetation indices against field measurements of biomass using broad vegetation classes to grid the spatial density of carbon across several forest types globally (Goetz et al., 1990, Hansen et al., 2013). In semi-arid ecosystems, given the low fractional cover of vegetation and heterogeneous landscape composition, this approach often results in large uncertainties in biomass estimation. The use of higher spatial resolution remote sensing data from passive sensors such as Quickbird and WorldView afford the delineation of individual crowns, with measurable properties such as crown area used to drive existing ground based allometries again via regression (Eckert et al., 2012). These approaches generally use tree size metrics limited to area or perimeter, often leveraging the spectral

signal afforded by the aforementioned passive sensors (Asner et al (2003)) or time series of archived aerial imagery (Browning et al (2008)). In semi-arid ecosystems however the degree of vegetation clumping often results in segments or patches either containing a single stem, or clumps of individuals. Further, validation data in such studies are normally comprised of stand-alone trees, or clumps of trees that often do not match each segment or patch precisely, often citing a minimum vegetation separation distance (Mirik et al (2013)). In the highly clumped and structurally complex ecosystems characteristic of semi-arid biomes, the variability in vegetation growth morphology and clumping is therefore very challenging to quantify and incorporate into estimates of AGB using passive sensors alone. The information afforded by active sensors such as airborne lidar can directly measure the structural characteristics of individual tree crowns, permitting the regression of structural parameters with existing ground based allometrics to estimate biomass (e.g.,Means et al., 2008 Næ sset and Gobakken 2008). Generally however, scaling these approaches to larger spatial extents still requires the delineation, or segmentation, of individual tree crowns in order to drive existing allometric relationships which in turn are driven by single tree measurements of height and/or stem diameter. In spite of the direct measurement of vegetation structure afforded by lidar, segmentation in highly clumped ecosystems is still a difficult task given that multiple individuals often present what appears to be a single crown volume when viewed remotely, or even on the ground. Here we tested the ability of aerial lidar data to drive existing allometric relationships for Juniperus monosperma, one seed juniper, in a juniper savanna in central New Mexico. This species is ideal for developing solutions of AGB measurement in semi-arid woodlands in the southwestern US. Juniperus spp. are found in juniper savanna and piñon and juniper dominated biomes (PJ woodlands) that together occupy 18 million ha in NM, CO, ZA and UT. Historically, the range of J. monosperma has extended into lower elevations during periods of available moisture ((**??**)). At the upper end of their elevation range, in PJ woodlands, juniper have become an increas-

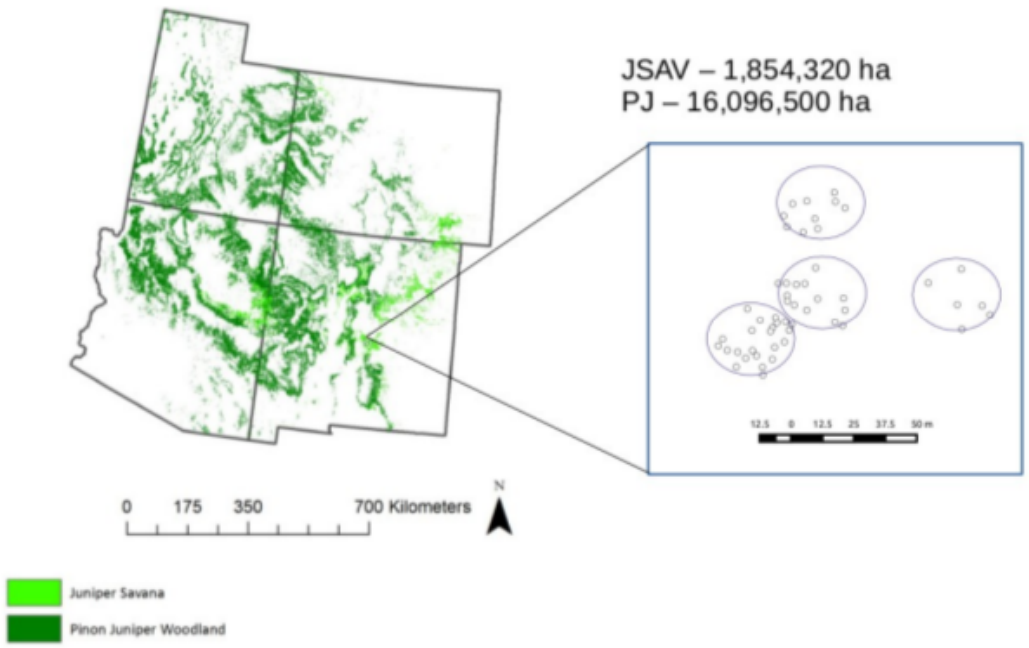


Figure 4.1: (A) Extent of pinon juniper woodlands (dark green) and juniper savanna (light green) ecosystems across the four corner states. (B) Location and layout of the field site, with tree crown locations bounded by the four 17.5 m radius circle plots.

ingly important component of the biome as multi-year droughts in the 1950s, turn of the century (1999-2002), trigger differential mortality of piñon (Allen et al, 2010; Breshears and Rich, 1997; Clifford et al, 2008, 2013). Most Juniperus spp. have a complicated growth morphology which resembles a large bush rather than a tree, with multiple woody stems which branch either just below or just above the ground. The high degree of clumping of the vegetation typical of Juniperus spp. dominated biomes further complicates the remote estimation of the vegetation, by increasing the aforementioned challenges associated with individual crown delineation.

We formed two hypotheses related to leveraging full 3D point cloud from lidar data to predict AGB in J. monosperma. First, the complex clumping patterns char-

acteristic of juniper dominated systems and the associated complications in crown delineation can be circumvented by segmenting multiple crowns into single clumps. Secondly, by computing statistics from the full 3D lidar point cloud instead of a canopy height model (CHM), lidar derived structural metrics will have a strong statistical relationship with field measured canopy properties, and subsequently AGB.

## 4.2 Methods

### 4.2.1 Site description

Our study site is located in a juniper savanna woodland, 24 km southeast of Willard, NM (34.425489, -105.861545). With a soil type of Penistaja fine sandy loam, the 4 ha study region exists within a managed rangeland ecosystem, with one seed juniper (J. monosperma) as the only woody species present. The study site exists as part of a larger gradient of ecological research sites referred to as the New Mexico Elevation Gradient (Anderson-Teixeira et al, 2011) for a description of the gradient, as well as site specific instrumentation).

### 4.2.2 Field measurements

The canopy dimensions of all J. monosperma over 1 m in height in four 17.5 meter radius circle plots were measured annually at this site from 2007-2014. We mapped the location of 52 individuals in these circle plots using a Trimble GPS having 40 cm location uncertainty (Figure 1). We measured canopy height, canopy area and canopy volume, as well as the diameter of the root crown of each tree to drive the existing allometric relationship for J. monosperma generated by (Grier et al, 1992).

Canopy height was measured using a collapsible height stick, and recorded as

Figure 4.2: Example growth morphology of a typical oneseed juniper. The multiple branching in this example occurs above the ground level.

the maximum height of each individual. Crown area was calculated by measuring the widest diameter and corresponding orthogonal dimension. Crown volume then was calculated given the height and subsequent projected area of the ellipsoid. Stem diameter of J. monosperma is challenging to measure given the complex growth morphology of individuals. The bole of the tree can either branch above or below the ground, making measurements of the root collar inconsistent if conducted at ground level (e.g., Figure 2). Diameter at breast height (dbh) is often impractical to estimate on this species given that height results in increasingly complex branching patterns. However, the allometry from (Grier et al, 1992) specifies the equivalent stem diameter (ESD, eqn 1) be recorded at the root collar. Therefore we chose to measure the stem diameter of individuals by idealizing a hemisphere centered at the base of the tree with a radius of 30 cm. In this manner, the woody mass often found at the base of the junipers which branch above ground would not bias the

ESD measurements.

$$\sqrt{\sum_{i=1}^{n} RCD_i^2} \tag{4.1}$$

Linear regression between sets of ground-based parameters of individual canopy dimensions (crown height, crown area, and crown volume) was used to determine the best predictor of ESD using the adjusted $R^2$ as the fit statistic.

### 4.2.3 Airborne lidar data

On September 8, 2011, high resolution aerial lidar was flown across a 6.5 km2 area situated along a 5 km north-south extent that included our 4 ha study area. Using an Optech Gemini with a laser pulse repetition rate of 125 kHz, 50% flightline overlap, scan angle of +/- 16 degrees and flying at an average altitude of 400 m above ground, lidar data were collected over the juniper savanna site. . The lidar point cloud data had an average horizontal point spacing of 20 cm, and a point density of 10 points $m^{-2}$. The mean horizontal relative accuracies was 25 cm And vertical accuracy was approximately 10 cm or better for open surfaces. Figure 3a shows the full analysis extent.

### 4.2.4 Canopy segementation and statistics

A digital terrain model (DTM) was extracted using the Terrain Extraction and Segmentation (TEXAS) software developed by the University of Texas Applied Research Laboratories ((Stevenson et al, 2013). The utilization of an accurate terrain model is critical for developing statistics based on relative heights above the ground surface. Once a digital terrain model (DTM) was generated, the individual points within the lidar point cloud were analyzed and labeled into general landcover categories such as

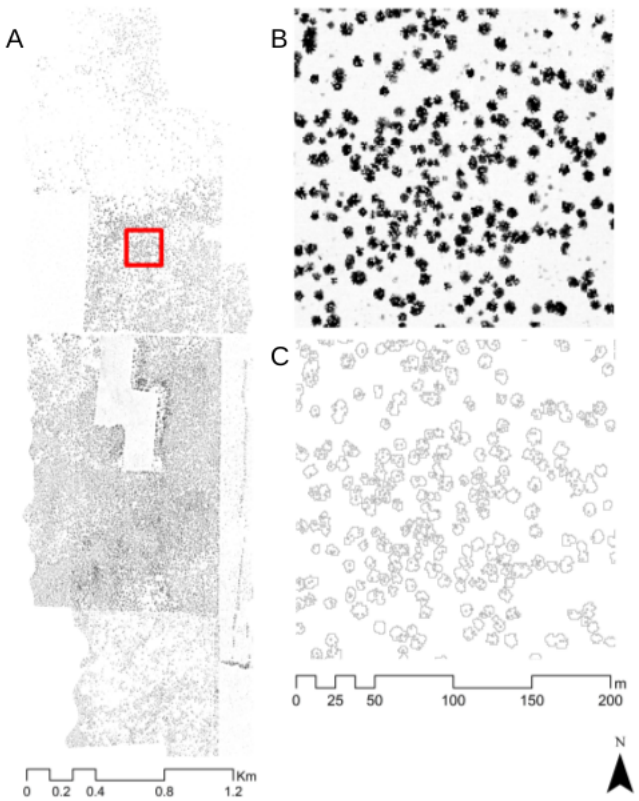


Figure 4.3: Lidar canopy height acquisition extent (A) with the 4 hectare study region identified by the extent indicator (B). The corresponding TEXPERT segmentation (C) delineated isolated and clumped crowns.

vegetation, terrain, or man-made surfaces (Figure 4a) using the TEXas Point cloud Exploitation Research Toolbox (TEXPERT) developed at the Applied Research Laboratories.

Lidar points labeled as vegetation were then grouped into segments based upon their Euclidean distance to matching adjacent points. For this project, vegetation points were grouped as a segment if a neighboring vegetation point was within 1 m (eg., Figure 4b). Height statistics computed on the lidar points within each segment include the standard metrics (i.e., mean, max, median, and standard deviation of height (m)). Other segment statistics included projected canopy area (m2), perimeter

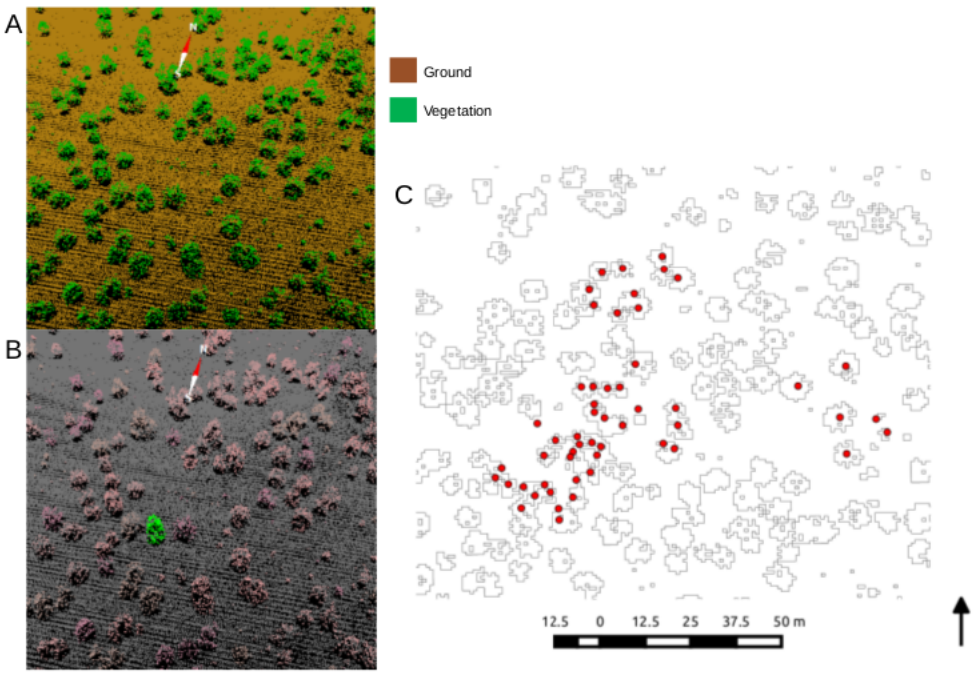


Figure 4.4: (A) The automatic delineation of ground and vegetation from TEXAS model, resulting in (B) clumped crown segmentation which was then (C) vectorized and overlayed on ground measured stem maps within our study area for segment statistic generation.

(m), canopy volume (m3), canopy density (points m-3), canopy closure (unitless), and eccentricity (unitless). Canopy volume, albeit an approximation, is defined as the projected canopy area multiplied by the maximum canopy height. Canopy closure is defined as the ratio of canopy photons to ground photons within the projected area of each segment. If a segment has a well-defined major and minor axis, the eccentricity is computed for each segment. Trees and clumps with a near circular shape should have an eccentricity near zero, whereas more elliptical shaped trees and clumps will have eccentricities near 0.5 or so. Again, the strength of these metrics is that they are computed on all the points within the segmented point cloud rather than the first reflective surface from a canopy height model. A vectorized version of the segmentation (i.e., the perimeter of each clump) was then produced and

overlayed with the ground based tree location data (Figure 4c).The maximum height from each tree crown within the field measured circle plots were manually retrieved and regressed against the corresponding field heights to assess the uncertainty in the ground  lidar height relationship. To further test how spatially representative our field measurement area was, we assessed the lidar derived max canopy heights by running a 7 x 7 kernel local maximum filter across the analysis extent and comparing the resulting distribution of heights against the field collected height data.

### 4.2.5 Validation of clump level allometrics

We scaled our estimates of stem diameter to the remote sensing data (i.e the lidar-derived segmentation) using the regression between ESD and single tree crown volume derived from the ground measurements. Given that our lidar segmentation approach delineated either stand alone or small clumps of trees, we needed to determine the ability of our regressions to predict the cumulative stem diameters of our ground validation trees. We visually inspected the GPS collected tree locations to associate segmented canopy objects with the corresponding ground validation data. In some cases, lidar-derived canopy segments included trees that were not sampled within the four 17.5 meter radius circle plots, reducing our effective sample size. Consequently, these individual trees and associated lidar derived segments were removed from the training set to avoid biasing the regression. For the remaining trees, the cumulative crown volumes and stem diameters were calculated and regressed against the lidar-derived segmented approximations. Given that the lidar-derived segment volumes are estimated from the projected segment area and the maximum height within each segment, we added canopy closure and canopy density computed on a per segment basis as additional covariates to the linear regression.

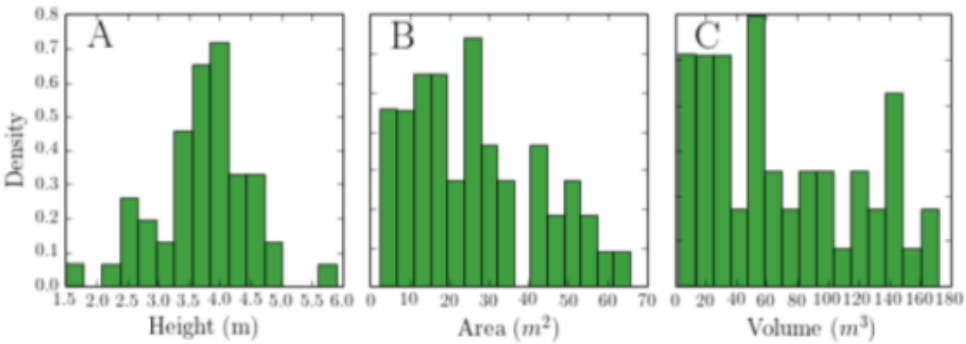


Figure 4.5: Distributions of juniper canopy parameters retrieved via ground measurement.

### 4.2.6 Uncertainty analysis

We adopted a simplified Monte-Carlo approach to error estimation, adapted from (**?**), when driving our field based allometries with remotely acquired crown properties. We used the regression standard error from the segment volume to segment ESD linear fit as well as the published standard error of prediction from the allometry for J. monosperma from (Grier et al, 1992) as our sources of error. For each crown segment we then computed 1000 realizations of segment ESD with random perturbations in the error term drawn from a normal distribution. Each of the 1000 realizations was then used to generate estimates of biomass, with the associated allometric uncertainty randomly perturbed in the same manner. In this way the mean biomass of each segment was calculated from a mean of 1000 model runs, and the associated standard deviation of each segment was leveraged as the uncertainty in biomass prediction.

## 4.3 Results

### 4.3.1 Field Measurements

The mean canopy height, area, and volume were 3.7 m, 26.2 m2, and 70.6 m3 respectively, with an estimated stem density within our 4 hectare analysis region of 135.1 stems ha-1 (Figure 5). The representativeness of the trees used to parametrize the lidar based regressions of biomass was assessed by comparing field measured canopy height with the mean local maximum canopy height within the lidar analysis extent, suggesting the distribution of heights measured by our field plots represents well the analysis extent (Figure 6). The mean estimated field biomass using the allometry from (Grier et al, 1992) was 15.6 Mg C ha-1. Regressions between ESD, which drives the allometry, and the three measured crown properties height, area and volume all performed well as predictors of single tree ESD, with adjusted $R^2$ values of 0.59, 0.77, and 0.79 respectively (p ¡ 0.001). Given that our objective for this study was to build a regression that allowed single crowns or the aggregation of multiple crowns per segment, we selected canopy volume as our predictor of ESD (Figure 7) which was the best predictor of ESD (RMSE = 1.23 cm2). The resulting regression equation was:

$$log(ESD) = 0.893 * log(Volume) + 7.825 \tag{4.2}$$

### 4.3.2 Lidar Segmentation

The TEXPERT derived segmentation identified a total of 3655 objects, each representing one or several crowns within the analysis extent (see Table 1 for summary statistics for entire region). The TEXPERT segmentation resulted in very few instances where a single crown was incorrectly segmented into multiple objects. The

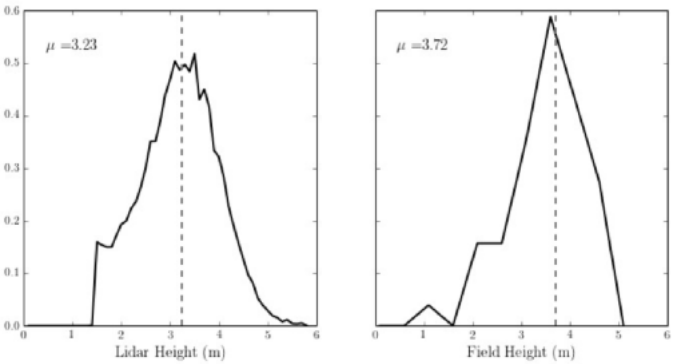


Figure 4.6: Distributions of tree heights from the imagery extent (left) and the Field validation plots (right). A vertical dashed line marks the mean (mu) of each Distribution.

majority of adjacent crowns (separation less than 1 meter) were clumped and segmented together. Large segments had a higher likelihood of containing multiple individuals, but in the case of the 4 ha region used for ground validation the number of individuals per segment was not significantly explained by segment volume, perimeter, or area. Contiguous swaths of vegetation tended to segment together, given that the segmentation was driven on the similarity of canopy height. While the number of cases was very small (7), several segments generated using this approach had a projected area greater than 1 ha, and a corresponding volume greater than 5,000 m3. Within our ground validation region, the arrangement of ground mapped individuals within segmented clumps corresponded well with the segmentation, where stand alone individuals were properly segmented, and overlapping crowns were grouped accordingly (e.g., Figure 4c). The four 17.5 meter radius circle plots contained a total of 19 segmented crown objects, composed of 52 individuals.

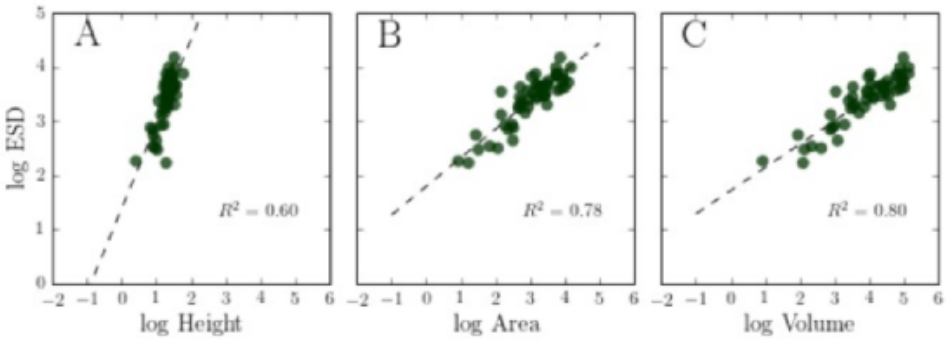


Figure 4.7: Ground derived relationships between equivalent stem diameter (see eqn. 1), and three remotely retrievable canopy parameters. Both axes have been log transformed to generate linear fits.

### 4.3.3 Segmentation derived biomass and uncertainty

We used linear regression to relate field measured canopy height with the corresponding manually retrieved lidar heights (Figure 8), with a RMSE of 0.60 m using the field measured height as the validation data. The field measurement data was clumped according to the corresponding segments in which the field measured crowns were located and the cumulative ESD per clump was calculated. This cumulative ESD was then regressed against the predicted ESD following the field measurement derived regression in equation 2 (Figure 9a; adjusted $R^2 = 0.83$, p $< 0.001$, RMSE = 4.12 cm2). Including segment canopy closure or segment canopy density as covariates in the regression significantly improved the fit (Figure 9b,c). The best fitting regression chosen to modify predicted ESD used segment density as a regression parameter (adjusted $R^2 = 0.91$, p $< 0.001$, RMSE = 3.26 cm2):

$$ESD = 1.93(ESDp) + 123.26(Density)2.25(ESDp * Density) \tag{4.3}$$

The resulting equation estimated total biomass over the field measurement extent of 15.9 +/- 0.4 Mg ha-1 compared to the field measured mean of 15.6 Mg ha$^{-1}$.

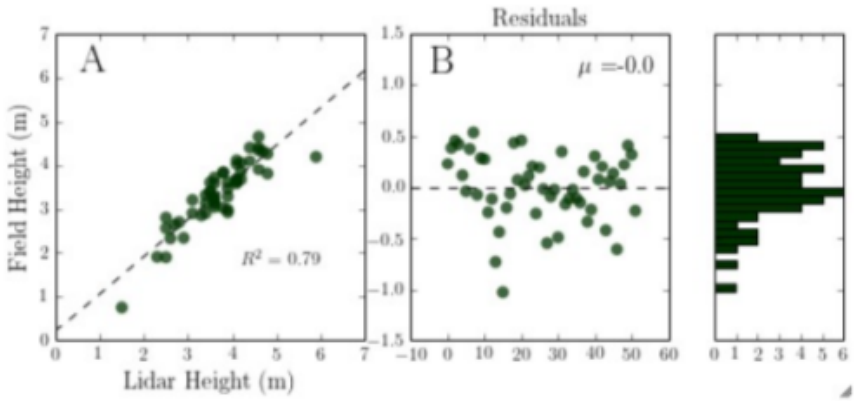


Figure 4.8: Field estimates of canopy height for the 52 trees sampled in The study. Lidar heights were manually extracted from the corresponding Crowns.

Given the propagation of error throughout the analysis incorporated both the remote prediction of ESD as well as the allometric uncertainty in AGB prediction, the relationship between segment AGB standard deviation followed an exponential relationship with mean segment AGB (Figure 10). Across the analysis extent, the distribution of biomass and consequently uncertainty is strongly a function of segment size, influenced primarily by continuity in structural features of the canopy such as stem density and variability in canopy height. The resulting mapped biomass il-

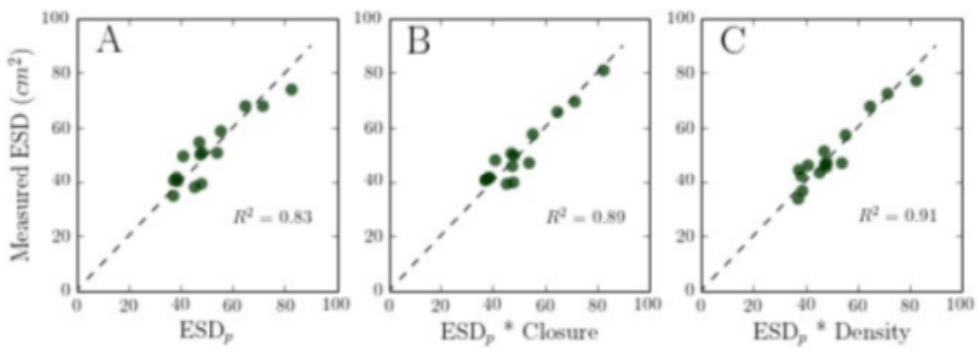


Figure 4.9: Remotely retrieved crown clump equivalent stem density (ESD) regressed against measured stem density within each clump (A) with canopy closure (B) and canopy density (C) as regression covariates.

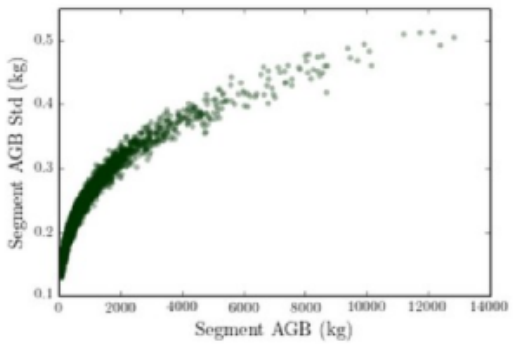


Figure 4.10: Relationship between the estimated segment biomass and the corresponding Monte-Carlo derived estimation of segment biomass standard deviation.

lustrates both the results of AGB mean and standard deviation resampled to 35 meter hexagonal cells (Figure 11 a,b) as well as the segment specific values for the entire validation region (Figure 11 c,d).

## 4.4 Discussion

We showed the scaling of the measured equivalent stem diameter (ESD) between individuals as a function of lidar derived segment volume produced estimations of above ground biomass (AGB) that matched single tree allometry derived predictions. Further, using canopy object density as a covariate to constrain the ESD VOLUME relationship not only improved the statistical power of the model but also clarified the conceptual model relationship, as:

$$ESD = SegmentVolume * SegmentDensity \tag{4.4}$$

Therefore, the ability of canopy object closure and segment density derived from the lidar point cloud increased the quality of the relationship between field measured and clump estimated ESD (Figure 9), which improved with the additional

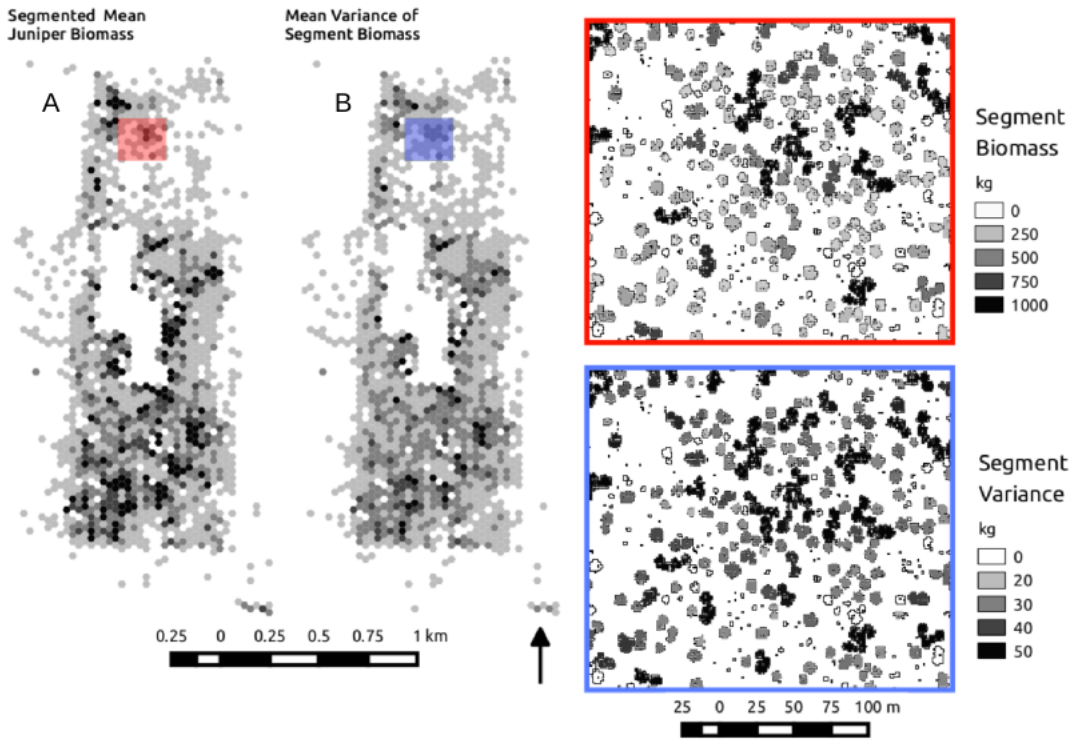


Figure 4.11: Mean (A) and Variance (B) of segment biomass across the analysis extent, spatially averaged for visualization. Corresponding detail subsets of individual segment mean and variance (C and D respectively).

parameter in spite of increasing model complexity (adjusted $R^2$ of 0.88). Our field measurements of j. monosperma were highly representative of the entire analysis extent, given the similarities in single crown maximum height (Figure 6). Further, the similarity between the lidar derived heights and the field measured heights for the 52 trees measured in this study showed good agreement, ($R^2$ of 0.79, $p < 0.001$). Potential sources of error between field measured crown parameters and those derived from lidar are potentially due to the horizontal vertical of the lidar data (1 m) effectively smoothing maximum heights and canopy edges. Higher resolution data may constrain the absolute error associated with measuring canopy heights but agreement to field measurements may not improve unless the sophistication of the

field height estimates increases (e.g. with the use of a laser hypsometer rather than a collapsible height stick). Our sample size for the regressions used to assess the goodness of fit at the segmentation level was greatly reduced relative to our ground validation sample size (n = 52 for field regressions, n = 15 for segmentation based regressions) given that in most cases single canopy objects derived from the lidar were actually comprised of multiple individuals. Further, our circle plot based validation approach poorly accommodated segmented canopy objects which spanned the circle plot perimeter, reducing the number of segments we were able to include in the predictive models. The relationship we developed between crown volume and equivalent stem diameter (ESD, eqn 2), corresponds well for our field measured trees, with nearly 90% of the variance in ESD explained by canopy volume. This seemed intuitive given the morphology of the trees (Figure 2) which grow more like large shrubs in this ecosystem. The complication in scaling this relationship using the lidar-derived segments is that the segmentation produces only crown shaped objects when the vegetation is isolated on the landscape. In many instances however, juniper grows in clumps often comprised of several trees. By using structural metrics derived from the lidar 3D point cloud such as canopy volume, canopy density, and canopy closure, we showed that the cumulative ESD and subsequently AGB agreed well with field measured estimates for a vegetation clump. This agreement demonstrates that a single tree segmentation may not be required to estimate biomass in juniper dominated ecosystems. Due to the fact that the segmentation was actually conducted on the full 3D point cloud however, each canopy object carried with it a host of ancillary data (Table 1) which our data show greatly reduced the need for single tree segmentation. Unfortunately, we did not test this for arbitrarily large segments, and presumable the scaling of single crown allometrics across increasingly large canopy objects will increase the uncertainty of the estimation. However, the TEXPERT segmentation process performed consistently in sparse, clumped systems, constraining the variability in segment size across the scene.

| Segment Statistic | Minimum | Maximum | Mean | StDev |
|---|---|---|---|---|
| Max Elevation (m) | 0.80 | 8.31 | 4.14 | 0.77 |
| Min Elevation (m) | 0.00 | 3.44 | 0.30 | 0.10 |
| Avg Elevation (m) | 0.10 | 5.66 | 2.12 | 0.40 |
| Med Elevation (m) | 0.00 | 7.36 | 2.26 | 1.07 |
| Std Elevation (m) | 0.17 | 2.37 | 1.02 | 0.23 |
| RMS Elevation (m) | 0.39 | 5.77 | 2.35 | 0.41 |
| Perimeter (m) | 10.97 | 243.94 | 41.91 | 23.46 |
| Projected Area ($m^2$) | 12.66 | 1112.36 | 92.36 | 103.74 |
| Volume ($m^3$) | 41.33 | 5857.98 | 387.49 | 517.76 |
| Density ($pts/m^3$) | 0.10 | 0.99 | 0.45 | 0.21 |
| Closure (unitless) | 0.17 | 1.00 | 0.75 | 0.15 |

Table 4.1: Summary of the clumped segmentation statistics generated from the full 3D point cloud for all of the canopy objects within the analysis extent.

The use of active sensors such as airborne lidar historically has improved the remote estimate of above ground biomass by relating destructive harvesting with plot scale measurements of height or fractional cover of vegetation. Often, this approach also hinges on individual tree crown delineation, and the resulting segment statistics are used as coefficients in a regression against the harvested biomass. In highly clumped vegetation, such as PJ woodlands or juniper savannas, the accuracy of single tree segmentation is difficult to quantify, and consequently scaling relationships designed for single crowns may be introducing systematic errors to the biomass estimation if for instance multiple woody boles are lumped into a single crown volume or tree segment height estimate. Our results suggest that the use of a segmentation conducted on the full 3D point cloud can still produce accurate estimates of AGB while permitting the clumping of vegetation to drive existing allometric relationships. While the motivation for this work stemmed from the complexity of remotely

estimating biomass in juniper dominated systems, juniper co-dominated woodlands (e.g., PJ woodlands) are by comparison far more complex. Mixed species allometries are inherently less accurate than their single species counterparts, but remotely leveraging single species allometries in a structurally complex ecosystem like a PJ woodland would require the ability to not only delineate crowns consistently, but also identify the difference between juniper and piñon. This approach therefore has the greatest utility in ecosystems dominated by single species, where the clumping of vegetation precludes the accurate segmentation of single crowns across the landscape.

## 4.5 Conclusions

Rapid and accurate remotely sensed estimations of ecosystem AGB is now more than ever a critical component to climate mitigation strategies in the southwestern US. Given the spatial extent of Juniperus spp. across the region, and the complex growth morphology exhibited by the genus, improving our ability to estimate the AGB of juniper dominated systems will provide valuable information about a range of ecosystems that will potentially undergo significant changes in structure at the ecosystem scale. Our case study in a juniper savanna showed the ability of lidar data to drive existing stem diameter based allometries remotely, using an object based approach. Given that delineating individual crowns in systems characterized by highly clumped vegetation is a challenging and error prone process, we scaled ground derived allometries based on crown volume to segmented groups of individuals. By driving the segmentation process on the full 3D point cloud data from lidar, we were able to refine the regression between segment volume and stem diameter using the density of points per segment. This work illustrated the capability of using segmentation approaches which delineated groups of individuals rather than single crowns to scale existing AGB allometric relationship at the regional scale. While

we believe this approach can both simplify the typical demand for crown level segmentation, and constrain AGB prediction uncertainty by leveraging 3D statistics per canopy segment, more work will be required to apply the technique in mixed species, highly clumped ecosystems such as PJ woodlands.

# Chapter 5

# Conclusions

The imminent transition of the climate in the Southwestern US to hotter, drier, and more variable conditions Seager et al (2012), coupled with the current sensitivity of the woody vegetation across the region (Williams et al, 2012; Clifford et al, 2013), necessitates rapid and accurate monitoring methods to aid with climate mitigation strategies at a national scale. This dissertation addresses the utility of high spatial resolution sensors in describing landscape transitions following piñon mortality and how those observation fall within the context of conventional sensors(Chapter 2), what implications the observed structural changes have on improving remotely driven carbon uptake modeling (Chapter 3), and finally how the above ground carbon stocks across these landscapes can be quickly quantified (Chapter 4).

In Chapter 2 we utilized a time series of high spatial resolution satellite imagery from RapidEye (5 x 5 meter pixels) to track the structural changes occurring in a simulated mortality event in 4 ha of piñon-juniper (PJ) woodlands in central NM. We compared the ability of the RapidEye sensor to track site-wide vegetation indices (VI) as indicators of canopy health, with the conventional, moderate resolution Landsat 7 ETM+ (30 x 30 meter pixels), and while both sensors detected signifncant side-wide

differences by the end of the second year, RapidEye afforded us the ability to track cover-type specific responses to the mortality. Two key findings of the work were that the piñon mortality resulted in the heterogeneous response of the understory greening up under the dead tree crowns, but not under the live trees or between trees, and that this pattern increased the sensitivity of the site-wide VI to changes in soil moisture.

In Chapter 3 we used the findings from Chapter 2 to attempt to constrain the uncertainty in regional carbon modeling of semi-arid ecosystems. We created a simple linear model hierarchy to determine if the normalized difference red-edge index (NDRE) would perform better than the conventional normalized difference vegetation index (NDVI), in standardized linear models using light and air temperature as the abiotic drivers. We also incorporated the normalized difference wetness index (NDWI) as a covariate in the hierarchy to assess whether or not information about canopy and surface moisture would reduce model error during periods of moisture limitation. We determined that while NDRE was significantly better at predicting GPP than NDVI when using RapidEye, the Landsat 7 ETM+ derived NDVI performed better all around. We believe that while NDRE has potential to constrain model error in these ecosystems, given its established improved sensitivity to changes in leaf area and chlorophyll over NDVI, the variability in view angle geometry from the RapidEye time series imposed more variability from scene to scene than the actual phenology at the sites. Finally, NDWI from Landsat ETM+ improved model fit in all cases, suggesting some metric of surface moisture is an essential component of vegetation modeling in semi-arid biomes.

In Chapter 4 we investigated the use of aerial lidar data to estimate the biomass of j. monosperma at the plot and regional scales. Typically in this region, the biomass of individual trees can be estimated by measuring the equivalent cross sectional area of the root crown, namely the equivalent stem diameter (Grier et al, 1992). We

showed that ESD was well explained by canopy volume, and consequently used segmentation of the full 3D point cloud data to generate canopy objects across the full analysis extent, calculating the object volume for each object. One major finding of the work was that while the segmentation of individual crowns is often an inaccurate and poorly validated step in most remote sensing approaches to biomass estimation, the cumulative crown volume per each canopy object scaled linearly with the cumulative ESD per object, letting us drive the existing ground based allometries from segment volume. Secondly, given that segment volumes tend to overestimate the true cumulative crown volume per segmented object, we showed that the density of lidar points per each segment further constrained error in the regression, allowing more predictive power and less uncertainty. While we did not harvest any biomass destructively during this study for absolute validation, we showed with a known degree of uncertainty how well we can predict existing allometries for highly clumped, juniperous ecosystems.

The body of work that comprises this dissertation contributes to our understanding of how semi-arid ecosystems respond structurally and functionally to mortality events, and addresses some of the challenges inherent to viewing those changes using remote sensing across large extents. While there is no replacement for in-situ measure of changes in canopy structure and function, the use of remote sensing to scale those relationships up to the landscape and region in semi-arid biomes plays a pivotal role in constraining the uncertainties associated with our understanding of current and future carbon-climate relationships.

# References

Abuzar M, Sheffield K, Whitfield D, O'connell M, McAllister A (2014) Comparing inter-sensor NDVI for the analysis of horticulture crops in south-eastern Australia. American Journal of Remote Sensing 2(1):1–9, DOI 10.11648/j.ajrs.20140201.11, URL http://article.sciencepublishinggroup.com/pdf/10.11648.j.ajrs.20140201.11.pdf

Adams H, Macalady A, Breshears DD, Allen CD, Stephenson N, Saleska S, Huxman T, McDowell N (2010) Climate- Induced Tree Mortality : Earth System Consequences. Eos, Transactions ... 91(17):2009–2011, URL http://onlinelibrary.wiley.com/doi/10.1029/2010EO170003/abstract

Allen CD, Macalady AK, Chenchouni H, Bachelet D, McDowell N, Vennetier M, Kitzberger T, Rigling A, Breshears DD, Hogg ET, Gonzalez P, Fensham R, Zhang Z, Castro J, Demidova N, Lim JH, Allard G, Running SW, Semerci A, Cobb N (2010) A global overview of drought and heat-induced tree mortality reveals emerging climate change risks for forests. Forest Ecology and Management 259(4):660–684, DOI 10.1016/j.foreco.2009.09.001, URL http://linkinghub.elsevier.com/retrieve/pii/S037811270900615X

Anderson-Teixeira KJ, Delong JP, Fox AM, Brese DA, Litvak ME (2011) Differential responses of production and respiration to temperature and moisture drive the carbon balance across a climatic gradient in New Mexico. Global Change Biology

17(1):410–424, DOI 10.1111/j.1365-2486.2010.02269.x, URL http://onlinelibrary.wiley.com/doi/10.1111/j.1365-2486.2010.02269.x/full

Asner GP, Heidebrecht KB (2002) Spectral unmixing of vegetation, soil and dry carbon cover in arid regions: Comparing multispectral and hyperspectral observations. International Journal of Remote Sensing 23(19):3939–3958, DOI 10.1080/01431160110115960, URL http://www.tandfonline.com/doi/abs/10.1080/01431160110115960

Asner GP, Archer S, Hughes RF, Ansley RJ, Wessman Ca (2003) Net changes in regional woody vegetation cover and carbon storage in Texas Drylands, 1937-1999. Global Change Biology 9(3):316–335, DOI 10.1046/j.1365-2486.2003.00594.x, URL http://doi.wiley.com/10.1046/j.1365-2486.2003.00594.x

Breshears D, Rich P (1997) Overstory-imposed heterogeneity in solar radiation and soil moisture in a semiarid woodland. Ecological Applications 4(7):1201–1215, URL http://www.esajournals.org/doi/abs/10.1890/1051-0761(1997)007[1201:OIHISR]2.0.CO;2

Breshears DD, Barnes FJ (1999) Interrelationships between plant functional types and soil moisture heterogeneity for semiarid landscapes within the grassland / forest continuum : a unified conceptual model. Landscape Ecology 14:465–478

Breshears DD, Cobb NS, Rich PM, Price KP, Allen CD, Balice RG, Romme WH, Kastens JH, Floyd ML, Belnap J, Anderson JJ, Myers OB, Meyer CW (2005) Regional vegetation die-off in response to global-change-type drought. Proceedings of the National Academy of Sciences of the United States of America 102(42):15,144–15,148

Browning DM, Archer SR, Asner GP, McClaran MP, Wessman Ca (2008) Woody plants in grasslands: post-encroachment stand dynamics. Ecological applications

: a publication of the Ecological Society of America 18(4):928–44, URL http://www.ncbi.nlm.nih.gov/pubmed/18536253

Canty M, Nielsen A (2008) Automatic radiometric normalization of multitemporal satellite imagery with the iteratively re-weighted MAD transformation. Remote Sensing of Environment 112(2008):1025 – 1036, DOI 10.1016/j.rse.2007.07.013, URL http://www.sciencedirect.com/science/article/pii/S0034425707003495

Choat B, Jansen S, Brodribb TJ, Cochard H, Delzon S, Bhaskar R, Bucci SJ, Feild TS, Gleason SM, Hacke UG, Jacobsen AL, Lens F, Maherali H, Martínez-Vilalta J, Mayr S, Mencuccini M, Mitchell PJ, Nardini A, Pittermann J, Pratt RB, Sperry JS, Westoby M, Wright IJ, Zanne AE (2012) Global convergence in the vulnerability of forests to drought. Nature 491(7426):752–5, DOI 10.1038/nature11688, URL http://www.ncbi.nlm.nih.gov/pubmed/23172141

Chojnacky DC, Heath LS, Jenkins JC (2013) Updated generalized biomass equations for North American tree species. Forestry 87(1):129–151, DOI 10.1093/forestry/cpt053, URL http://forestry.oxfordjournals.org/cgi/doi/10.1093/forestry/cpt053

Clifford M, Rocca M, Delph R (2008) Drought induced tree mortality and ensuing Bark beetle outbreaks in Southwestern pinyon-juniper woodlands. USDA Forest Service Proceedings pp 39–51, URL http://citeseerx.ist.psu.edu/viewdoc/download?doi=10.1.1.165.4291\&rep=rep1\&type=pdf\#page=49

Clifford M, Royer P, Cobb N (2013) Precipitation thresholds and droughtinduced tree dieoff: insights from patterns of Pinus edulis mortality along an environmental stress gradient. New . . . pp 413–421, URL http://onlinelibrary.wiley.com/doi/10.1111/nph.12362/full

Colgan MS, Asner GP, Swemmer T (2013) Harvesting tree biomass at the stand level to assess the accuracy of field and airborne biomass estimation in savan-

nas. Ecological applications : a publication of the Ecological Society of America 23(5):1170–84, URL http://www.ncbi.nlm.nih.gov/pubmed/23967584

Coops NC, Waring RH, Wulder Ma, White JC (2009) Prediction and assessment of bark beetle-induced mortality of lodgepole pine using estimates of stand vigor derived from remotely sensed data. Remote Sensing of Environment 113(5):1058–1066, DOI 10.1016/j.rse.2009.01.013, URL http://linkinghub.elsevier.com/retrieve/pii/S003442570900025X

Detto M, Montaldo N, Albertson JD, Mancini M, Katul G (2006) Soil moisture and vegetation controls on evapotranspiration in a heterogeneous Mediterranean ecosystem on Sardinia, Italy. Water Resources Research 42(8):1–16, DOI 10.1029/2005WR004693, URL http://www.agu.org/pubs/crossref/2006/2005WR004693.shtml

Edburg SL, Hicke JA, Brooks PD, Pendall EG, Ewers BE, Norton U, Gochis D, Gutmann ED, Meddens AJH (2012) Cascading impacts of bark beetle-caused tree mortality on coupled biogeophysical and biogeochemical processes. Frontiers in Ecology and the Environment 10(8):416–424, DOI 10.1890/110173, URL http://www.esajournals.org/doi/pdf/10.1890/110173

Eitel JU, Gessler PE, Smith AM, Robberecht R (2006) Suitability of existing and novel spectral indices to remotely detect water stress in Populus spp. Forest Ecology and Management 229(1-3):170–182, DOI 10.1016/j.foreco.2006.03.027, URL http://linkinghub.elsevier.com/retrieve/pii/S0378112706002283

Eitel JU, Vierling La, Litvak ME, Long DS, Schulthess U, Ager Aa, Krofcheck DJ, Stoscheck L (2011) Broadband, red-edge information from satellites improves early stress detection in a New Mexico conifer woodland. Remote Sensing of Environment 115(12):3640–3646, DOI 10.1016/j.rse.2011.09.002, URL http://linkinghub.elsevier.com/retrieve/pii/S0034425711003294

Eitel JUH, Long DS, Gessler PE, Hunt ER, Brown DJ (2009) Sensitivity of Ground-Based Remote Sensing Estimates of Wheat Chlorophyll Content to Variation in Soil Reflectance. Soil Science Society of America Journal 73(5):1715, DOI 10.2136/sssaj2008.0288, URL https://www.soils.org/publications/sssaj/abstracts/73/5/1715

Elmore AJ, Mustard JF, Manning SJ, Lobell DB (2000) Quantifying Vegetation Change in Semiarid Environments : Precision and Accuracy of Spectral Mixture Analysis and the Normalized Difference Vegetation Index 102(January):87–102

Fensholt R, Langanke T, Rasmussen K, Reenberg A, Prince SD, Tucker C, Scholes RJ, Le QB, Bondeau A, Eastman R, Epstein H, Gaughan AE, Hellden U, Mbow C, Olsson L, Paruelo J, Schweitzer C, Seaquist J, Wessels K (2012) Greenness in semi-arid areas across the globe 19812007 an Earth Observing Satellite based analysis of trends and drivers. Remote Sensing of Environment 121:144–158, DOI 10.1016/j.rse.2012.01.017, URL http://linkinghub.elsevier.com/retrieve/pii/S0034425712000545

Flanagan L, Wever L, Carlson P (2002) Seasonal and interannual variation in carbon dioxide exchange and carbon balance in a northern temperate grassland. Global Change Biology 8:599–615, URL http://onlinelibrary.wiley.com/doi/10.1046/j.1365-2486.2002.00491.x/full

Gamon J, Peñuelas J, Field C (1992) A narrow-waveband spectral index that tracks diurnal changes in photosynthetic efficiency. Remote Sensing of Environment 41(1):35–44, DOI 10.1016/0034-4257(92)90059-S, URL http://linkinghub.elsevier.com/retrieve/pii/003442579290059S

Gamon Ja, Serrano L, Surfus JS (1997) The photochemical reflectance index: an optical indicator of photosynthetic radiation use efficiency across species, functional types, and nutrient levels. Oecologia 112(4):492–501, DOI 10.1007/s004420050337,

URL http://www.springerlink.com/openurl.asp?genre=article\&id=doi:10.1007/s004420050337

Gibbs HK, Brown S, Niles JO, Foley Ja (2007) Monitoring and estimating tropical forest carbon stocks: making REDD a reality. Environmental Research Letters 2(4):045,023, DOI 10.1088/1748-9326/2/4/045023, URL http://stacks.iop.org/1748-9326/2/i=4/a=045023?key=crossref.4118e8af5a9a3ac02c1bb32f8a92c50f

Gitelson A, Merzlyak M (1996) Signature analysis of leaf reflectance spectra: algorithm development for remote sensing of chlorophyll. Journal of plant physiology 148:494–500, URL http://www.sciencedirect.com/science/article/pii/S0176161796802847

Gitelson A, Vina A, Ciganda V, Rundquist DC (2005) Remote estimation of canopy chlorophyll content in crops. Geophysical Research ... 32:4–7, DOI 10.1029/2005GL022688, URL http://www.agu.org/pubs/crossref/2005/2005GL022688.shtml

Grier C, Elliott K, McCullough D (1992) Biomass distribution and productivity of Pinus edulisJuniperus monosperma woodlands of north-central Arizona. Forest Ecology and Management 50:331–350, URL http://www.sciencedirect.com/science/article/pii/037811279290346B

Hsieh Ci, Katul G, Chi Tw (2000) An approximate analytical model for footprint estimation of scalar uxes in thermally strati ed atmospheric ows. Advances in water resources 23:765–772

Huang C, Asner G, Martin R, Barger NN, Neef JC (2009) Multiscale analysis of tree cover and aboveground carbon stocks in pinyon-juniper woodlands. Ecological Applications 19(3):668–681, URL http://www.esajournals.org/doi/abs/10.1890/07-2103.1

Huang Cy, Asner GP, Barger NN, Neff JC, Floyd ML (2010) regional aboveground live carbon losses due to drought-induced tree dieback in pinon-juniper ecosystems. Remote Sensing of Environment 114(7):1471–1479, DOI 10.1016/j.rse.2010.02.003, URL http://dx.doi.org/10.1016/j.rse.2010.02.003

Huang Cy, Asner G, Barger N (2012) Modeling regional variation in net primary production of pinyonjuniper ecosystems. Ecological Modelling 227:82–92, DOI 10.1016/j.ecolmodel.2011.12.016, URL http://dx.doi.org/10.1016/j.ecolmodel.2011.12.016http://www.sciencedirect.com/science/article/pii/S0304380011006041

aR Huete, Jackson R, Post D (1985) Spectral response of a plant canopy with different soil backgrounds. Remote Sensing of Environment 17(1):37–53, DOI 10.1016/0034-4257(85)90111-7, URL http://linkinghub.elsevier.com/retrieve/pii/0034425785901117

Huete AR (1988) A soil-adjusted vegetation index (savi). Remote Sensing of Environment 25(25):53–70, DOI 10.1016/j.rse.2010.02.003, URL http://dx.doi.org/10.1016/j.rse.2010.02.003

Huxman TE, Snyder KA, Tissue D, Leffler AJ, Ogle K, Pockman WT, Sandquist DR, Potts DL, Schwinning S (2004) Precipitation pulses and carbon fluxes in semiarid and arid ecosystems. Oecologia 141(2):254–268, DOI 10.1007/s00442-004-

IPCC (2007) Climate change 2007: The physical science basis. Tech. rep., 1535 pp.

IPCC (2014) Climate change 2014: The physical science basis. Tech. rep., 1535 pp.

Jenkins JC, Chojnacky DC, Heath LS, Birdsey RA (2003) National-scale biomass estimators for United States tree species. Forest Science 49(1):12–35, URL http://www.ingentaconnect.com/content/saf/fs/2003/00000049/00000001/art00002

Jr PSC (1988) An improved dark-object subtraction technique for atmospheric scattering correction of multispectral data. Remote Sensing of Environment 24(3):459

– 479, DOI http://dx.doi.org/10.1016/0034-4257(88)90019-3, URL http://www.sciencedirect.com/science/article/pii/0034425788900193

Kennedy R, Cohen W, Schroeder T (2007) Trajectory-based change detection for automated characterization of forest disturbance dynamics. Remote Sensing of Environment 110:370 – 386, DOI 10.1016/j.rse.2007.03.010, URL http://www.sciencedirect.com/science/article/pii/S0034425707001216

Kennedy RE, Yang Z, Cohen WB (2010) Remote Sensing of Environment Detecting trends in forest disturbance and recovery using yearly Landsat time series : 1 . LandTrendr  Temporal segmentation algorithms. Remote Sensing of Environment 114(12):2897–2910, DOI 10.1016/j.rse.2010.07.008, URL http://dx.doi.org/10.1016/j.rse.2010.07.008

Krofcheck DJ, Eitel JU, Vierling La, Schulthess U, Hilton TM, Dettweiler-Robinson E, Pendleton R, Litvak ME (2014) Detecting mortality induced structural and functional changes in a piñon-juniper woodland using Landsat and RapidEye time series. Remote Sensing of Environment 151:102–113, DOI 10.1016/j.rse.2013.11.009, URL http://linkinghub.elsevier.com/retrieve/pii/S0034425713004203

Larson KM, Small EE, Gutmann ED, Bilich AL, Braun JJ, Zavorotny VU (2008) Use of GPS receivers as a soil moisture network for water cycle studies. Geophysical Research Letters 35(24):L24,405, DOI 10.1029/2008GL036013, URL http://doi.wiley.com/10.1029/2008GL036013

Lasslop G, Reichstein M, Papale D, Richardson AD, Arneth A, Barr A, Stoy P, Wohlfahrt G (2010) Separation of net ecosystem exchange into assimilation and respiration using a light response curve approach: critical issues and global evaluation. Global Change Biology 16(1):187–208, DOI 10.1111/j.1365-2486.2009.02041.x, URL http://doi.wiley.com/10.1111/j.1365-2486.2009.02041.x

Leuning R, Cleugh Ha, Zegelin SJ, Hughes D (2005) Carbon and water fluxes over a temperate Eucalyptus forest and a tropical wet/dry savanna in Australia: measurements and comparison with MODIS remote sensing estimates. Agricultural and Forest Meteorology 129(3-4):151–173, DOI 10.1016/j.agrformet.2004.12.004, URL http://linkinghub.elsevier.com/retrieve/pii/S0168192305000079

Li X, Gao Z, Bai L, Huang Y (2012) POTENTIAL OF HIGH RESOLUTION RAPIDEYE DATA FOR SPARSE VEGETATION. Geoscience and Remote Sensing Symposium (IGARSS), 2012 IEEE International pp 420–423

Liu S, Bond-Lamberty B, Hicke J (2011) Simulating the impacts of disturbances on forest carbon cycling in North America: Processes, data, models, and challenges. Journal of Geophysical . . . 116:1–22, DOI 10.1029/2010JG001585, URL http://www.lter.uaf.edu/pdf/1543_Liu_Bond-Lamberty_2011.pdf

McDowell NG (2011) Mechanisms linking drought, hydraulics, carbon metabolism, and vegetation mortality. Plant physiology 155(3):1051–9, DOI 10.1104/pp.110.170704, URL http://www.pubmedcentral.nih.gov/articlerender.fcgi?artid=3046567\&tool=pmcentrez\&rendertype=abstract

Mirik M, Chaudhuri S, Surber B, Ale S, Ansley R (2013) Evaluating Biomass of Juniper Trees (Juniperus pinchotii) from Imagery-Derived Canopy Area Using the Support Vector Machine Classifier 2(June):181–192, URL http://file.scirp.org/Html/16-2630027_33224.htm

Monteith JL (1972) Solar Radiation and Productivity in Tropical Ecosystems. The Journal of Applied Ecology 9(3):747–766

Monteith JL, Moss CJ (1977) Climate and the Efficiency of Crop Production in Britain [and Discussion]. Philosophical Transactions of the Royal Society B: Biological Sciences 281(980):277–294, DOI 10.1098/rstb.1977.0140, URL http://rstb.royalsocietypublishing.org/cgi/doi/10.1098/rstb.1977.0140

Muldavin E, Moore D, Collins S (2008) Aboveground net primary production dynamics in a northern Chihuahuan Desert ecosystem. Oecologia 155(1):123–132, DOI 10.1007/s00442-007-0880-2, URL http://www.springerlink.com/index/P4G70R458W237135.pdf

Næ sset E, Gobakken T (2008) Estimation of above- and below-ground biomass across regions of the boreal forest zone using airborne laser. Remote Sensing of Environment 112(6):3079–3090, DOI 10.1016/j.rse.2008.03.004, URL http://linkinghub.elsevier.com/retrieve/pii/S0034425708000849

Nielsen Aa, Conradsen K, Simpson JJ (1998) Multivariate Alteration Detection (MAD) and MAF Postprocessing in Multispectral, Bitemporal Image Data: New Approaches to Change Detection Studies. Remote Sensing of Environment 64:1–19

Poulter B, Frank D, Ciais P, Myneni RB, Andela N, Bi J, Broquet G, Canadell JG, Chevallier F, Liu YY, Running SW, Sitch S, van der Werf GR (2014) Contribution of semi-arid ecosystems to interannual variability of the global carbon cycle. Nature 509(7502):600–3, DOI 10.1038/nature13376, URL http://www.ncbi.nlm.nih.gov/pubmed/24847888

Qi J, Chehbouni A, Huete A (1994) A modified soil adjusted vegetation index. Remote Sensing of . . . 48:119–126, URL http://www.sciencedirect.com/science/article/pii/0034425794901341

Rich PM, Breshears DD, White AB (2008) Phenology of Mixed Woody-Herbaceous Ecosystems following Extreme Events : Net and Differential Responses. Ecological Society of America 89(2):342–352

Rock B, Vogelmann J, Williams D (1986) Remote detection of forest damage. BioScience 36(7):439–445, URL http://www.jstor.org/stable/1310339

Roy DP, Ju J, Kline K, Scaramuzza PL, Kovalskyy V, Hansen M, Loveland TR, Vermote E, Zhang C (2010) Web-enabled Landsat Data (WELD): Landsat ETM+ composited mosaics of the conterminous United States. Remote Sensing of Environment 114(1):35–49, DOI 10.1016/j.rse.2009.08.011, URL http://linkinghub.elsevier.com/retrieve/pii/S0034425709002545

Royer PD, Cobb NS, Clifford MJ, Huang CY, Breshears DD, Adams HD, Villegas JC (2011) Extreme climatic event-triggered overstorey vegetation loss increases understorey solar input regionally: primary and secondary ecological implications. Journal of Ecology 99(3):714–723, DOI 10.1111/j.1365-2745.2011.01804.x, URL http://doi.wiley.com/10.1111/j.1365-2745.2011.01804.x

Running SW, Baldocchi DD, Turner DP, Gower ST, Bakwin PS, Hibbard KA (1999) A Global Terrestrial Monitoring Network Integrating Tower Fluxes , Flask Sampling , Ecosystem Modeling and EOS Satellite Data 127(April):108–127

Schwalm CR, Williams CA, Schaefer K, Baldocchi D, Black TA, Goldstein AH, Law BE, Oechel WC, U KTP, Scott RL (2012) Reduction in carbon uptake during turn of the century drought in western North America. Nature Geoscience 5(8):551–556, DOI 10.1038/ngeo1529, URL http://dx.doi.org/10.1038/ngeo1529

Seager R, Ting M, Held I, Kushnir Y, Lu J, Vecchi G, Huang HP, Harnik N, Leetmaa A, Lau NC, Li C, Velez J, Naik N (2007) Model projections of an imminent transition to a more arid climate in southwestern North America. Science (New York, NY) 316(5828):1181–4, DOI 10.1126/science.1139601, URL http://www.ncbi.nlm.nih.gov/pubmed/17412920

Seager R, Naik N, Vogel L (2012) Does Global Warming Cause Intensified Interannual Hydroclimate Variability?*. Journal of Climate 25(9):3355–3372, DOI 10.1175/JCLI-D-11-00363.1, URL http://journals.ametsoc.org/doi/abs/10.1175/JCLI-D-11-00363.1

Shaw J, Steed B, DeBlander L (2005) Forest Inventory and Analysis (FIA) annual inventory answers the question: What is happening to pinyon-juniper woodlands? Journal of Forestry 103(6):280–285, URL http://www.ingentaconnect.com/content/saf/jof/2005/00000103/00000006/art00004

Sims D, Rahman a, Cordova V, Elmasri B, Baldocchi D, Bolstad P, Flanagan L, Goldstein a, Hollinger D, Misson L (2008) A new model of gross primary productivity for North American ecosystems based solely on the enhanced vegetation index and land surface temperature from MODIS. Remote Sensing of Environment 112(4):1633–1646, DOI 10.1016/j.rse.2007.08.004, URL http://linkinghub.elsevier.com/retrieve/pii/S0034425707004105

Sims Da, Brzostek ER, Rahman AF, Dragoni D, Phillips RP (2014) An improved approach for remotely sensing water stress impacts on forest C uptake. Global change biology 20(9):2856–66, DOI 10.1111/gcb.12537, URL http://www.ncbi.nlm.nih.gov/pubmed/24464936

Spruce J, Sader S, Ryan R, Smoot J (2010) Assessment of MODIS NDVI time series data products for detecting forest defoliation by gypsy moth outbreaks. Remote Sensing of ... 115(2):427–437, DOI 10.1016/j.rse.2010.09.013, URL http://dx.doi.org/10.1016/j.rse.2010.09.013http://www.sciencedirect.com/science/article/pii/S0034425710002865

Stevenson TH, Magruder La, Neuenschwander AL, Bradford B (2013) Automated bare earth extraction technique for complex topography in light detection and ranging surveys. Journal of Applied Remote Sensing 7(1):073,560, DOI 10.1117/1.JRS.7.073560, URL http://remotesensing.spiedigitallibrary.org/article.aspx?doi=10.1117/1.JRS.7.073560

Stoms DM, Bueno MJ, Davis FW (1997) Viewing Geometry of AVHRR Image Composites Derived Using Multiple Criteria 63(6):681–689

Tucker C (1979) Red and photographic infrared linear combinations for monitoring vegetation. Remote sensing of Environment 8(2):127–150, URL http://www.sciencedirect.com/science/article/pii/0034425779900130

Wang Q, Adiku S, Tenhunen J, Granier A (2005) On the relationship of NDVI with leaf area index in a deciduous forest site. Remote Sensing of Environment 94(2):244–255, DOI 10.1016/j.rse.2004.10.006, URL http://linkinghub.elsevier.com/retrieve/pii/S0034425704003232

Webb E, Pearman GI, Leuning R (1980) Correction of flux measurements for density effects due to heat and water vapour transfer. Quarterly Journal of the . . . 106:85–100, URL http://onlinelibrary.wiley.com/doi/10.1002/qj.49710644707/abstract

Williams A, Allen C, Macalady A (2012) Temperature as a potent driver of regional forest drought stress and tree mortality. Nature Climate 3(1):8–13, DOI 10.1038/NCLIMATE1693, URL http://www.nature.com/nclimate/journal/vaop/ncurrent/full/nclimate1693.html

Williams aP, Allen CD, Millar CI, Swetnam TW, Michaelsen J, Still CJ, Leavitt SW (2010) Forest responses to increasing aridity and warmth in the southwestern United States. Proceedings of the National Academy of Sciences of the United States of America 107(50):21,289–94, DOI 10.1073/pnas.0914211107, URL http://www.pubmedcentral.nih.gov/articlerender.fcgi?artid=3003095\&tool=pmcentrez\&rendertype=abstract

Wulder M, White J, Bentz B, Alvarez M, Coops N (2006) Estimating the probability of mountain pine beetle red-attack damage. Remote Sensing of Environment 101(2):150–166, DOI 10.1016/j.rse.2005.12.010, URL http://linkinghub.elsevier.com/retrieve/pii/S0034425705004220

Yang J, Weisberg PJ, Bristow Na (2012) Landsat remote sensing approaches for monitoring long-term tree cover dynamics in semi-arid woodlands: Comparison of

vegetation indices and spectral mixture analysis. Remote Sensing of Environment 119:62–71, DOI 10.1016/j.rse.2011.12.004, URL http://linkinghub.elsevier.com/retrieve/pii/S003442571100441X

Yuan W, Liu S, Yu G, Bonnefond JM, Chen J, Davis K, Desai AR, Goldstein AH, Gianelle D, Rossi F, Suyker AE, Verma SB (2010) Global estimates of evapotranspiration and gross primary production based on MODIS and global meteorology data. Remote Sensing of Environment 114(7):1416–1431, DOI 10.1016/j.rse.2010.01.022, URL http://linkinghub.elsevier.com/retrieve/pii/S0034425710000556

Zhao M, Running S, Heinsch FA (2011) MODIS-Derived Terrestrial Primary Production. In: Ramachandran B, Justice CO, Abrams MJ (eds) Land Remote Sensing and Global Environmental Change, Remote Sensing and Digital Image Processing, vol 11, Springer New York, New York, NY, chap 28, pp 635–660, DOI 10.1007/978-1-4419-6749-7, URL http://www.springerlink.com/index/10.1007/978-1-4419-6749-7